NASA TECHNICAL NOTE

NASA TN D-4778

NASA TN D-4778

ANALYTICAL INVESTIGATION OF THERMAL DEGRADATION OF HIGH-PERFORMANCE MULTILAYER INSULATION IN THE VICINITY OF A PENETRATION

by William R. Johnson and Earl L. Sprague

Lewis Research Center
Cleveland, Ohio

NATIONAL AERONAUTICS AND SPACE ADMINISTRATION • WASHINGTON, D. C. • SEPTEMBER 1968

ANALYTICAL INVESTIGATION OF THERMAL DEGRADATION OF HIGH-PERFORMANCE MULTILAYER INSULATION IN THE VICINITY OF A PENETRATION

By William R. Johnson and Earl L. Sprague

Lewis Research Center
Cleveland, Ohio

NATIONAL AERONAUTICS AND SPACE ADMINISTRATION

For sale by the Clearinghouse for Federal Scientific and Technical Information
Springfield, Virginia 22151 – CFSTI price $3.00

ABSTRACT

An analytical investigation was conducted to determine the thermal degradation of high-performance multilayer insulation on a liquid hydrogen tank in the vicinity of a penetration. Results were obtained with and without the use of a thermal buffer zone between the shields and the penetration, for various values of thermal contact resistance. Input variables to the program included radiation source temperature, penetration diameter, number of shields, shield emissivity, shield thermal conductivity, shield spacing, buffer zone dimensions, and buffer zone thermal conductivity. The results of the program are presented in graphical form, as well as in equations representing curve fits of the analytical data.

ANALYTICAL INVESTIGATION OF THERMAL DEGRADATION OF HIGH-PERFORMANCE MULTILAYER INSULATION IN THE VICINITY OF A PENETRATION

by William R. Johnson and Earl L. Sprague

Lewis Research Center

SUMMARY

An analytical investigation was conducted to determine the direct lateral heat flow to a penetration, the net increase in heat flow into a tank, and the radius of the thermally degraded area created by the presence of a cylindrical pipe or tank support penetrating the multilayer insulation on a liquid hydrogen tank. The multilayer insulation system simulated by the analysis used nonconducting spacers between consecutive shields of 1/4-mil (0.00064-cm) double aluminized polyester film. The analytical model considered the multilayer insulation butted directly to the penetration, as well as butted against a thermal buffer zone placed between the shields and the penetration.

The resulting equations from the analysis were programmed for solution by a computer. Input variables to the program included radiation source temperature, penetration diameter, number of shields, shield emissivity, shield thermal conductivity, shield spacing, buffer zone dimensions, and buffer zone thermal conductivity. Various values of thermal contact resistance between the shields and the penetration or buffer zone were generated to make the analytical results applicable to the real case.

The results of the program are presented in graphical form to demonstrate the effect of any given variable on the thermal degradation of the insulation system. Specific values of the heat flows into the tank, for a particular penetration and insulation system, can be determined for any value of thermal contact resistance, with or without a buffer zone. In addition, curve fits of the analytical data yield equations which express the heat flows and degraded radius as functions of the input variables.

INTRODUCTION

High-performance multilayer insulation has been proposed to enable long-term storage of liquid hydrogen in space. The extremely low heat flux of such an insulation system is realized when the heat transfer normal to the shields is primarily by radiation. Such a system can be approximated by a large number of highly reflective shields (e.g., aluminized polyester film) separated by low thermal conductivity spacers (e.g., silk netting).

The thermal performance of multilayer insulation, however, can be seriously degraded in the area where a penetration such as a plumbing line or tank strut passes through the insulation blanket. To prevent any direct radiation from impinging on the tank itself, the individual shields must butt up against the penetration. A cross-sectional view of a five-shield multilayer insulation system and penetration is shown in figure 1(a). Using the minimum thickness of aluminum considered adequate to ensure a low emissivity surface, together with a low thermal conductivity substrate (polyester film), reduces the lateral thermal conductivity by a factor of 100 over the shield of pure aluminum. However, even the use of a minimum thickness of aluminum with its high thermal conductivity results in a relatively high thermal conductivity for the shield.

A technique proposed by several investigators (e.g., ref. 1) for minimizing the heat conducted laterally along the shields uses a thermal buffer zone between the penetration and the shields. A cross-sectional view of this configuration is shown in figure 1(b). Unlike the radiation shields, the buffer zone has the same thermal conductivity in both the normal and lateral directions. This conductivity would greatly exceed the effective thermal conductivity normal to the shields, but be less than the effective thermal conductivity of the shields in the lateral direction. Increasing the buffer zone width would decrease the lateral heat flow into the penetration. However, this might be offset by an increase in the normal heat flow into the tank.

The primary objectives of the analysis are to determine representative values for the direct lateral heat flow to a penetration, the net increase in heat flow into a tank, and the radius of the resulting thermally degraded area. The results of the program are intended to emphasize the potential magnitude of the problem, and as such can only be used as a guide to preliminary design considerations. For instance, a comparison of the no buffer zone configurations with those using a buffer zone establishes a range of values for the maximum thermal conductivity that a buffer zone material may possess and still warrant its use.

The analytical results obtained represent maximum values since thermal contact resistance in the form of a finite temperature differential at any junction could not be readily incorporated into the program. However, specifying artificial temperature profiles at the shield-penetration interface, or combining the results of the buffer region for one particular run (set of input data) with the results for the shield region of another run gave re-

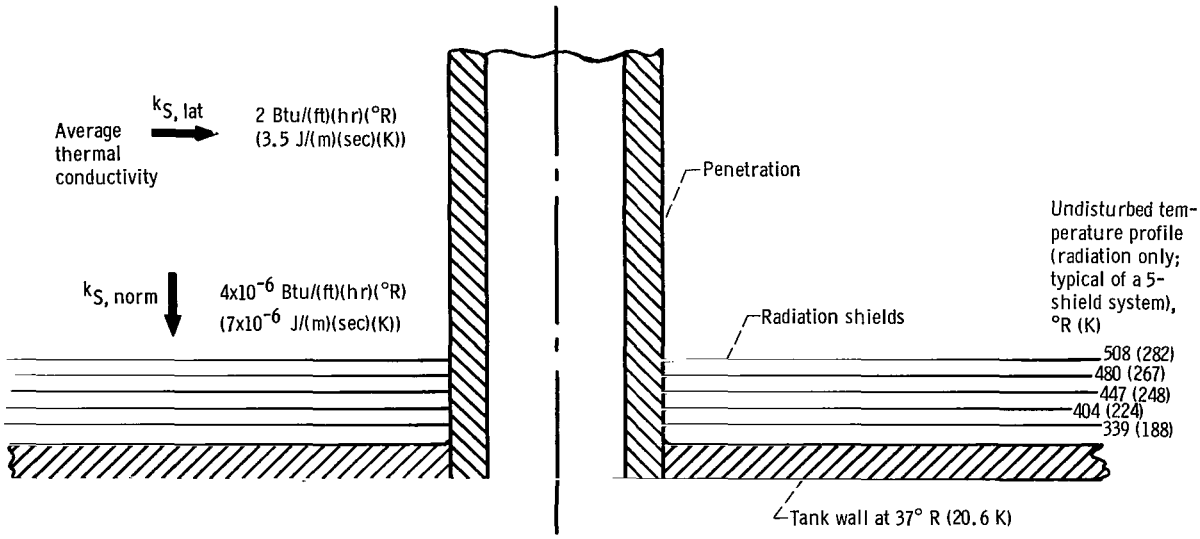

(a) Shields butted to penetration.

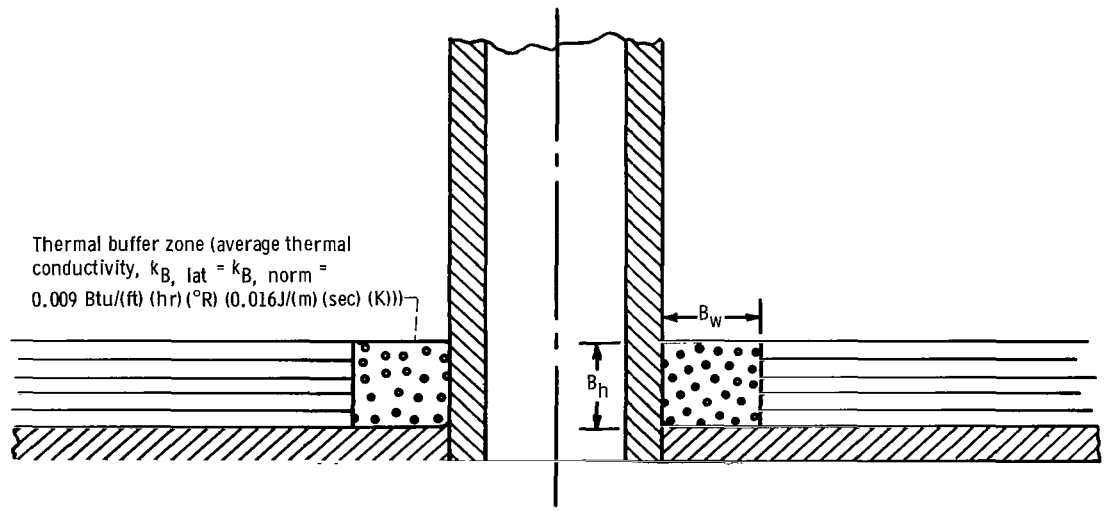

(b) Use of thermal buffer zone.

Figure 1. - Penetration model.

sults that simulated thermal contact resistance. The correction factors corresponding to various values of thermal contact resistance make the analytical results more descriptive of an actual application.

ANALYSIS

Shield-Penetration Model

The analytical model for a typical 30° angular segment of the insulation system having the shields butted against a penetration is shown in figure 2(a). A grid network of points is set up throughout the segment. The temperature profile at the penetration ($T_{p,1}$, $T_{p,2}$, . . ., $T_{p,N}$) is specified, and the temperature of the tank wall is set at 37° R (20.6 K). A temperature at each grid point is calculated by performing a heat balance about that point. The analysis considers only conduction in the radial direction and only radiation in the normal direction. The directions and modes of heat flows for a typical point ($T_{r,N-2}$) are indicated in figure 2(a). A converged temperature profile is obtained only after the temperatures have been adjusted so that a heat balance at each and every point is obtained. The heat flows conducted along each shield into the penetration and the radiation exchange between the shield adjacent to the tank and the tank itself are then readily determined.

The spacing between consecutive grid points in the radial direction could take on three different values for any particular run. The smallest grid increment (usually 0.5 in. or 1.3 cm) was used in the vicinity of the penetration where changes in the shield temperatures were most abrupt. The intermediate grid increment (1.0 in. or 2.5 cm) followed by the largest grid increment (2.0 in. or 5.1 cm) were conveniently set as multiples of the smallest grid increment. Several trial runs for 10 shields indicated no significant change in the temperature profiles, and thus the resulting heat-transfer rates, when the smallest grid was reduced to 0.25 or 0.125 inch (0.65 or 0.33 cm).

An acceptable solution for any given number of shields occurred when the calculated temperature profile at the edge of the model approached the undisturbed temperature profile ($T_{und,1}$, $T_{und,2}$, . . ., $T_{und,N}$). The undisturbed temperature profile is that profile occurring in a section of basic insulation without the penetration (i.e., no lateral heat transfer). The undisturbed temperature profile at the edge ensured that no lateral heat transfer occurred at this point. Hence, the entire thermally degraded area was located within the model.

As stated previously, the analysis considers heat transfer normal to the shields by radiation only, and laterally by conduction along the shields. For a given shield, the

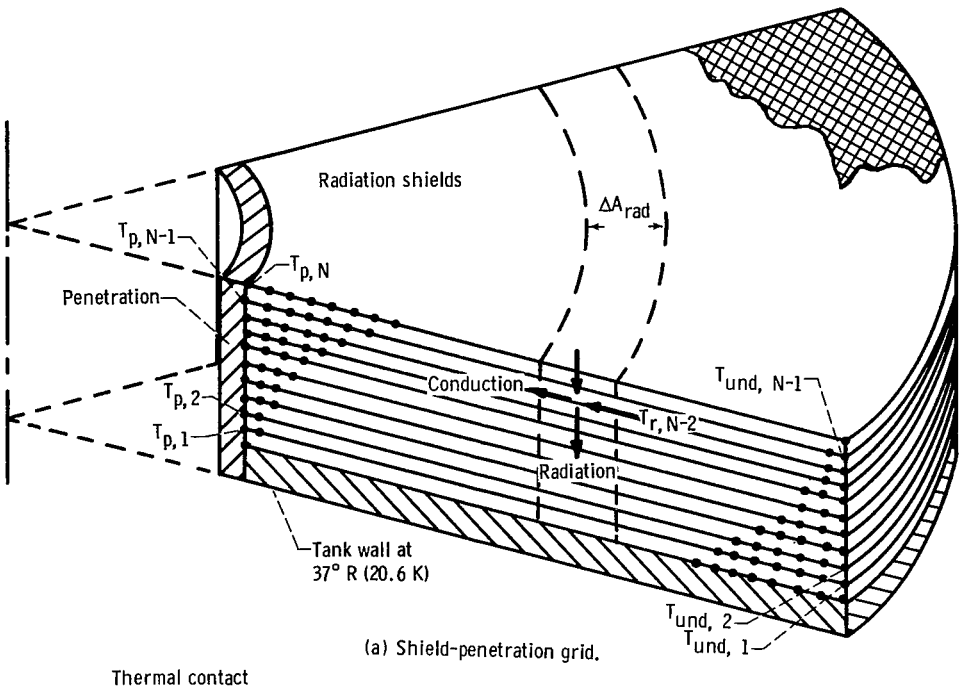

(a) Shield-penetration grid.

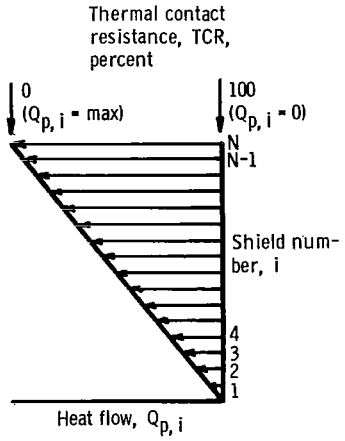

(b) Lateral heat flow to penetration.

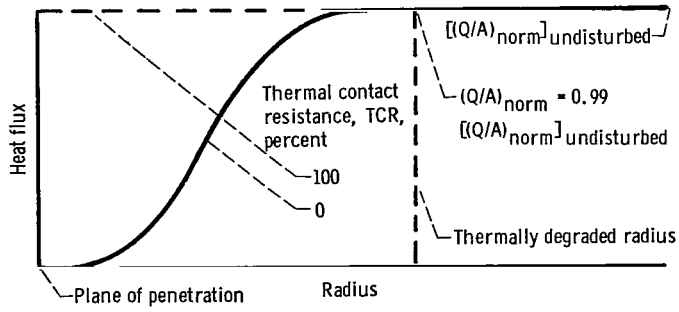

(c) Normal heat flux to tank wall $(Q/A)_{norm}$.

Figure 2. - Shield-penetration model.

conduction between two adjacent points is the familiar expression

$$Q_{cond} = k_S A_{cs,S} \frac{\Delta T}{\Delta r}$$

(All symbols are defined in appendix A.) For radiation, the particular temperature at a given grid point is considered to extend over the entire incremental radiation area (ΔA_{rad}) surrounding this point:

$$Q_{rad} = \Delta A_{rad} \sigma F_{i,i-1} \left(T_{i,r}^4 - T_{i-1,r}^4 \right)$$

Thus, as far as radiation is concerned, the temperature profile on any shield is a series of step changes in temperature.

The primary assumption in this analysis was that the spacer contribution to conduction in either direction is negligible. This assumption is partially validated by the experimental results (ref. 2) which show that, for an ideal installation using silk netting as the spacer material, conduction contributes only 20 percent of the overall heat transfer in the normal direction. This increase over pure radiation heat transfer can be simulated approximately by increasing the shield emissivity.

The primary reason for the assumption is, however, the lack of experimental data to enable a valid separation of conduction and radiation on a shield to shield basis. Conduction may not be a constant value between consecutive shields, but may be highly dependent on the temperature profile pure radiation would tend to establish. A theoretical calculation of the conduction term would require knowledge of the thermal conductivity against temperature and effective cross-sectional areas of the silk netting. These terms would be even more difficult to define for lateral conduction into the penetration. The final obstacle would involve determining how thermal contact resistance might decrease the conduction term. This thermal contact resistance would occur where the shields touch the spacer as well as where the spacer could butt against the penetration.

The real question is what difference the mode of heat transfer in the normal direction has on the results of the analysis. As long as the shield emissivity can be changed to vary the overall normal heat flow to simulate some conduction, the results appear valid. Using pure radiation heat transfer, as opposed to a combination of radiation and conduction (if a valid relation was available), may only tend to establish somewhat higher temperatures on the shields adjacent to the tank. The temperatures on the shields farthest from the tank will undoubtedly remain approximately the same for each case. Since these shields transfer the majority of the lateral heat, the total lateral heat conducted into this penetration remains essentially the same for each case. This is, of course, the parameter of primary concern.

The analysis makes two additional assumptions. First, the radiation view factor between corresponding incremental areas of consecutive shields is one. This is valid because of the relatively high length to gap ratio characteristic of infinitely long parallel plates. A shield spacing of 0.020 inch (0.051 cm) and a grid size of 0.5 inch (1.3 cm) offers a minimum length to gap ratio of 25. The second assumption assumes that shield emissivity is not a function of temperature. This assumption is made because experimental data for variations in emissivity of aluminized polyester film with temperature were not available. Because of the relatively high temperatures even in the shield adjacent to the tank, it can be shown that possible variations in emissivity will not significantly change the normal heat flux.

The direct lateral heat flow to the penetration ($Q_{p,\,lat}$) is defined as the sum of the individual shield heat flows ($Q_{p,\,i}$):

$$Q_{p,\,lat} = \sum_{i=1}^{N} Q_{p,\,i}$$

The individual heat flows should increase for those shields having a higher undisturbed temperature, as shown in figure 2(b).

The net increase in heat flow into the tank (ΔQ_p) must consider the decreased normal radiation in the vicinity of the penetration. The anticipated normal heat flux resulting from the reduced temperatures of the shield adjacent to the tank is shown in figure 2(c). The value of ΔQ_p was defined as the total quantity of heat transferred through an arbitrarily defined area A_{dist} surrounding the penetration minus that quantity transferred through the same area of undisturbed insulation:

$$\Delta Q_p = Q_{p,\,lat} + \sum_{A_{dist}} Q_{norm} - \left(\frac{Q}{A}\right)_{norm,\,und} A_{dist}$$

where A_{dist} is defined by the radius where the normal heat flux approaches 99 percent of the undisturbed heat flux $(Q/A)_{norm,\,und}$ (see fig. 2(c)).

The analytical program assumes a perfect thermal short between the shield edges and the penetration (i.e., no thermal contact resistance (TCR) is considered). This means that whatever temperature profile is imposed on the penetration is simultaneously imposed on the shield edges butting against the penetration. If the penetration is at liquid hydrogen temperature ($T_{p,\,1} = T_{p,\,2} = \ldots T_{p,\,N} = 37^{\circ}$ R (20.6 K)), $Q_{p,\,lat}$ is a maximum for which TCR is defined as zero. If the temperature profile imposed on the shield edges corresponded to the individual undisturbed shield temperatures ($T_{p,\,i} = T_{i,\,und}$,

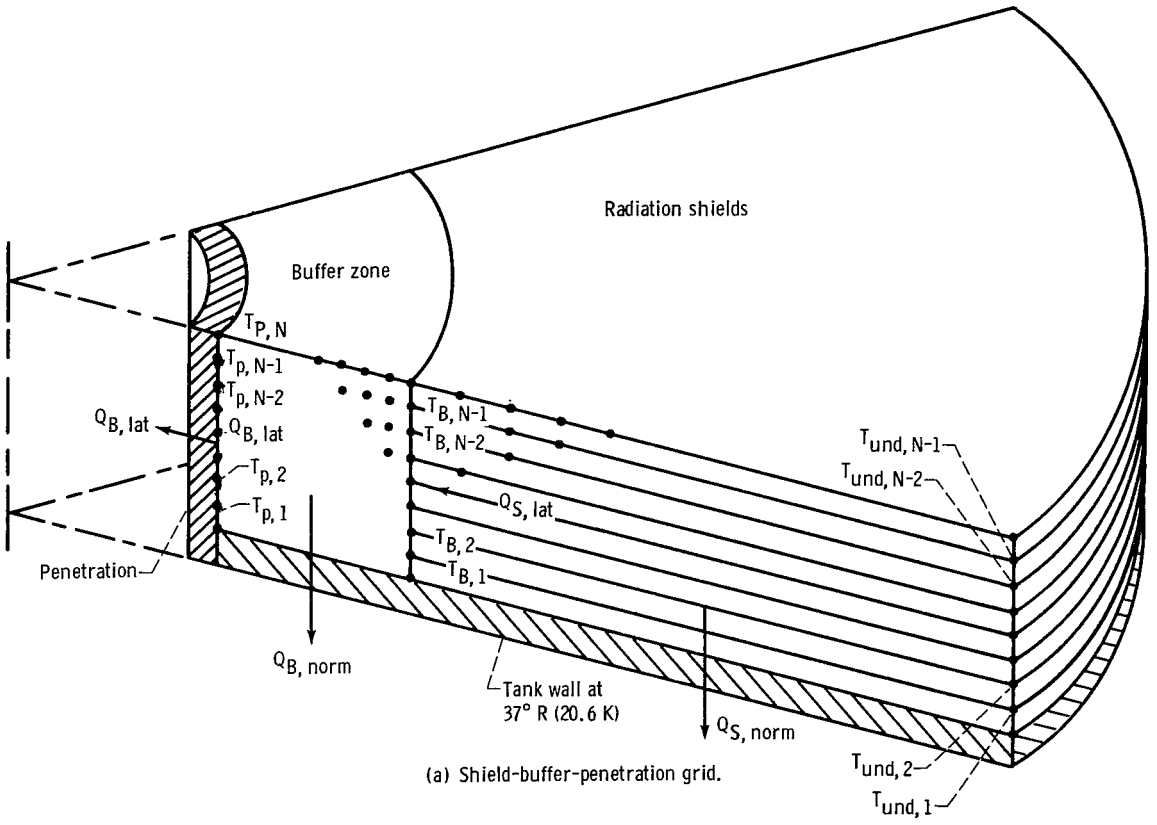

(a) Shield-buffer-penetration grid.

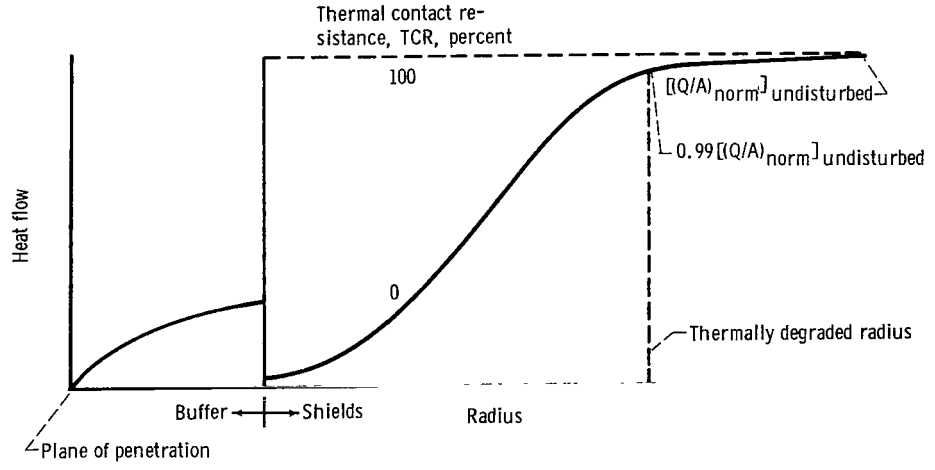

(b) Normal heat flux to tank wall $(Q/A)_{norm}$.

Figure 3. - Shield-buffer-penetration model.

where $i = 1, 2, \ldots, N$), $Q_{p, lat}$ would be zero - a condition for which TCR is defined as 100 percent.

The temperature difference across this interface, corresponding to a given value of TCR, determines the resulting heat flow across this interface. The transfer of higher lateral heat flows, associated with those shields exposed to higher undisturbed temperatures, requires a proportionately higher ΔT to be imposed at this interface. The analysis uses a given value of TCR to reduce the maximum available ΔT for each shield by a fixed percentage. All shield edge temperatures ($T_{p, i}$) for a given value of TCR can then be calculated in terms of their respective undisturbed temperatures ($T_{und, i}$) and liquid hydrogen temperature (T_{lh}). The only simplification here is that TCR remains constant for each shield of a given penetration insulation configuration:

$$TCR(\text{percent}) = 100 \frac{T_{p, i} - T_{lh}}{T_{und, i} - T_{lh}}$$

Shield - Buffer Zone - Penetration Model

The analytical model for a typical 30^{o} angular segment of the insulation system using a thermal buffer zone between the shields and the penetration is shown in figure 3(a). A grid network of points is set up in the buffer zone in addition to the previously described grid in the shield region. The buffer zone points are located in the same planes as the shields, and they generally had a radial spacing equal to the shield spacing. Again the temperatures are adjusted until a heat balance at each and every point is obtained. The heat flows out each surface of the insulation segment are then readily determined.

The emissivity of the top surface of the buffer zone was set equal to the emissivity of the shield in order to compute the radiation received by this surface. This can be duplicated in an actual application by attaching a shield section to the top of the buffer zone. This radiation and the heat conducted laterally from the shields are now redistributed into two components - that conducted laterally into the penetration ($Q_{B, lat}$) and that conducted into the tank in the normal direction ($Q_{B, norm}$). The total heat transferred out of the buffer zone ($Q_{B, tot}$) can then be expressed as

$$Q_{B, tot} = Q_{B, lat} + Q_{B, norm}$$

The net increase in heat flow into the tank ($\Delta Q_{p, B}$) must take into consideration the anticipated reduced normal heat flows in the shield region adjacent to the buffer zone as shown in figure 3(b). When an arbitrarily defined thermally degraded area ($A_{dist, B}$) is

used, $\Delta Q_{p,B}$ can be expressed as

$$\Delta Q_{p,B} = Q_{B,tot} + \sum_{A_{dist}} Q_{norm} - \left(\frac{Q}{A}\right)_{und} A_{dist}$$

where A_{dist} is again defined by the radius where the normal heat flux approaches 99 percent of the undisturbed heat flux.

The analysis assumed a perfect thermal short existed at all interfaces. An actual application would have some thermal contact resistance (TCR) at each of the various interfaces. For convenience, this analysis considered all of the TCR to occur at the buffer zone - shield interface. The error incurred in not considering TCR at the buffer zone - penetration or buffer zone - tank interfaces is only a matter of definition. The effect of TCR is to reduce heat flows through the buffer zone by imposing finite temperature differences at the interfaces considered. Whether or not the same decrease in heat flow is obtained by a series of temperature drops or by one temperature drop only changes the relation of TCR against ΔT at the interface in question.

Any specific thermal conductivity of the buffer zone material ($k_{B,avg}$) established a specific temperature profile at the buffer zone - shield junction. Various values of $k_{B,avg}$ were used with the same geometric configuration to generate different temperature profiles, and their corresponding lateral heat flows across this interface. Since this heat flow must be transferred through the buffer zone, a single interface temperature ($T_{int,avg}$) representative of a given profile was used to express the relation between this profile and its associated lateral heat flow:

$$Q_{S,lat} \propto k_{B,avg}(T_{int,avg} - T_{lh})$$

The lateral heat flow obtained with a low $k_{B,avg}$ buffer zone yields a certain $T_{int,avg,S}$ representative of the shield edge profile. This same lateral heat flow can be used with a higher $k_{B,avg}$ buffer zone to give a different $T_{int,avg,B}$ representative of the buffer edge temperature profile:

$$Q_{S,lat} \propto \left(k_{B,avg}\right)_{low}\left(T_{int,avg,S} - T_{lh}\right) \propto \left(k_{B,avg}\right)_{high}\left(T_{int,avg,B} - T_{lh}\right)$$

The theoretical temperature difference ($T_{int,avg,S} - T_{int,avg,B}$) divided by the maximum potential temperature difference available ($T_{und,S} - T_{int,avg,B}$) defines the value of TCR. A relation between TCR and the decreased heat flows is then readily determined.

Equations and Boundary Conditions

The equation governing the two-dimensional heat transfer in the buffer region (see fig. 4) is

$$\frac{\partial}{\partial r}\left[k_B(T)\frac{\partial T}{\partial r}\right] + \frac{\partial}{\partial z}\left[k_B(T)\frac{\partial T}{\partial z}\right] = 0 \tag{1}$$

and in the shield region the equation for the top shield is

$$\left.\begin{aligned} &W\frac{d}{dr}\left[rk_S(T)\frac{dT}{dr}\right] + r\sigma\left[F_{rs,N}T_{rs}^4 - (F_{rs,N} + F_{N,N-1})T_{N,r}^4 + F_{N,N-1}T_{N-1,r}^4\right] = 0 \\ &\text{and for all other shields } i, \text{ it is} \\ &W\frac{d}{dr}\left[rk_S(T)\frac{dT}{dr}\right] + r\sigma\left[F_{i,i+1}T_{i+1,r}^4 - (F_{i,i+1} + F_{i,i-1})T_{i,r}^4 + F_{i,i-1}T_{i-1,r}^4\right] = 0 \end{aligned}\right\} \tag{2}$$

These are the two differential equations to be solved. The solutions for both the no-buffer zone and buffer zone models must satisfy the following boundary conditions. Along the pipe wall at $r = R_p$ (fig. 4) the temperature is prescribed:

$$T(R_p, z) = T_p \tag{3}$$

where T_p is the local pipe temperature.

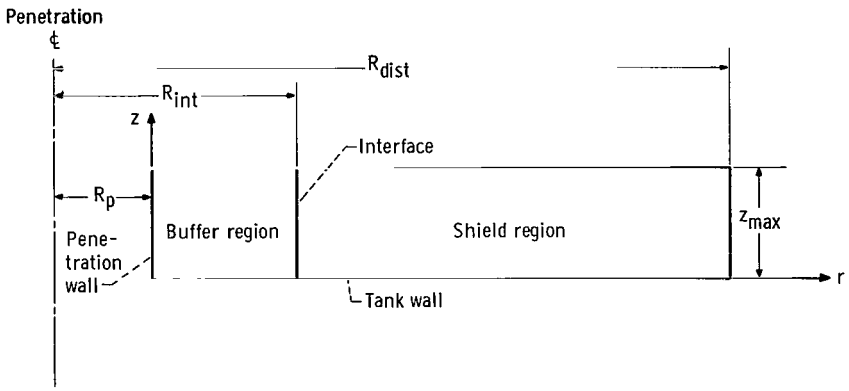

Figure 4. - Cross-sectional view of shield-buffer-penetration model.

The temperature along the tank surface at $z = 0$ is constant, so

$$T(r, 0) = T_{lh} \tag{4}$$

Since there is no heat flow across the line $r = R_{dist}$,

$$\left(\frac{dT}{dr}\right)_{r=R_{dist}} = 0 \tag{5}$$

On the surface of the top shield at $z = z_{max}$ there is radiation from space, so that in the shield region

$$Q_{z=z_{max}} = F_{rs,N}\sigma\left(T_{rs}^4 - T_{N,r}^4\right) \tag{6}$$

Boundary condition equations (7) and (8) apply to the buffer zone model only.

$$k_B\left(\frac{\partial T}{\partial z}\right)_{z=z_{max}} = F_{rs,N}\sigma\left(T_{rs}^4 - T_{N,r}^4\right) \tag{7}$$

where T_{rs} is the source temperature. There must be continuity of heat flow at the interface ($r = R_{int}$) between the buffer and shield regions; hence,

$$\left(k_B\frac{\partial T_B}{\partial r}\right)_{r=R_{int}} = \left(k_S\frac{dT_S}{dr}\right)_{r=R_{int}} \tag{8}$$

The equations were solved numerically on a digital computer using a finite-difference line-by-line overrelaxation method. Details of the numerical method of solution are given in appendix B.

Program Variables

The radiation shield simulated in the analysis was composed of a 1/4-mil-(0.00064-cm-) thick polyester film substrate having 600 Å of aluminum vapor deposited on each side. This was the only aluminum coating thickness used, since experimental data (ref. 2) indicated this as a minimum thickness to assure a low emissivity.

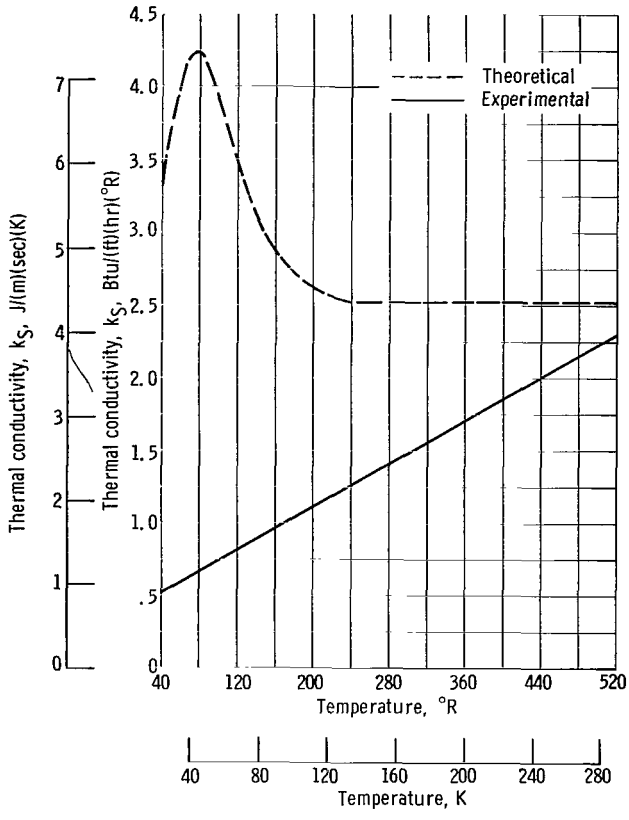

Figure 5. - Comparison of theoretical and experimental values of lateral thermal conductivity of a single radiation shield as function of temperature.

A shield emissivity of 0.024 was used for the majority of the data runs. However, values of emissivity up to 0.096 were used to determine what effect changing the normal radiation had on the magnitude of heat lost to the penetration. Increasing the normal radiation would be one way of simulating some conduction heat transfer normal to the shields that otherwise could not be considered. However, the lateral heat flows down the shields may be slightly biased, since changing the emissivity does not alter the resulting temperature profiles on the shields.

The analysis considered two distinct values (experimental and theoretical) for the thermal conductivity of the shield. As indicated in figure 5, a significant discrepancy between the two occurs over the lower temperature range. The theoretical value is the calculated effective weighted value of 0.00025 inch (0.00064 cm) of polyester film combined with the 1200 Å of aluminum, using the bulk thermal conductivity of 99.9-percent pure aluminum. The experimental value as determined by Lockheed (ref. 3) indicates the possibility that the thermal conductivity of thin films at low temperatures may deviate significantly from the bulk value. The difference is attributed to the effect that the electron

mean free path has on the thermal conduction properties. Theoretically this effect becomes extremely significant as the electron mean free path approaches the film thickness.

The number of shields used was varied from 5 to 160 for the shield penetration model, and from 5 to 80 for the thermal buffer zone configurations. Increasing the number of grid points in the analytical model for the higher number of shields increased the computer program time to the point where the cost in running more than 80 shields with a buffer zone became exorbitant. Since only radiation occurred in the normal direction for the shield penetration model, the individual shields could be clustered in groups of five. The emissivity of each group now acting as a single shield was adjusted so that the normal radiation in the undisturbed section of insulation remained unchanged. The effective thickness of the clustered shield was increased by a factor of five to determine the lateral conduction for the total number of shields simulated.

Clustering the shields was done for all shield-penetration configurations using 40 or more shields. Sufficient points were run comparing clustered to nonclustered configurations to establish the validity of the technique.

The shield spacing used in the shield-penetration model was immaterial, since heat transfer in the normal direction was by radiation only. When using the buffer zone configuration, however, the shield spacing was set at 0.020 and 0.010 inch (0.051 and 0.025 cm). This simulated the "best" and "worst" cases, respectively, for an actual application.

The penetration diameter was generally set at 2 inches (5.1 cm). However, sufficient runs were made to determine any performance changes due to changes in the diameter, both with or without the buffer zone.

The radiating source temperature was generally set at 520° R (289 K) to simulate the extreme case and to maximize the various heat flows being compared. Sufficient runs over the range of 200° to 520° R (111 to 289 K) were made to establish performance curves. The emissivity of the radiating source was set at 0.8 and the emissivity of the tank surface was set equal to the shield emissivity.

The average thermal conductivity of the buffer zone material was varied from 0.0004 to 0.0095 Btu per foot per hour per $^{\circ}$R (0.00069 to 0.0164 J/(m)(sec)(K)). The higher value is representative of a 2-pound-per-cubic-foot (32.04-kg/m^3) density polyurethane foam. The lower value typical of glass wool fibers represents the lowest practical value attainable.

In all buffer zone configurations the buffer zone height was set equal to the insulation thickness. The buffer zone width was varied from near zero to twice the buffer zone height.

RESULTS AND DISCUSSION

Case 1 - Shields Thermally Shorted to Penetration

The temperature profiles on the 1st, 10th, and 20th shields of a 20-shield system thermally shorted to a 2-inch- (5.1-cm-) diameter penetration at liquid hydrogen temperature are shown in figure 6. As shown the shield temperatures are severely degraded

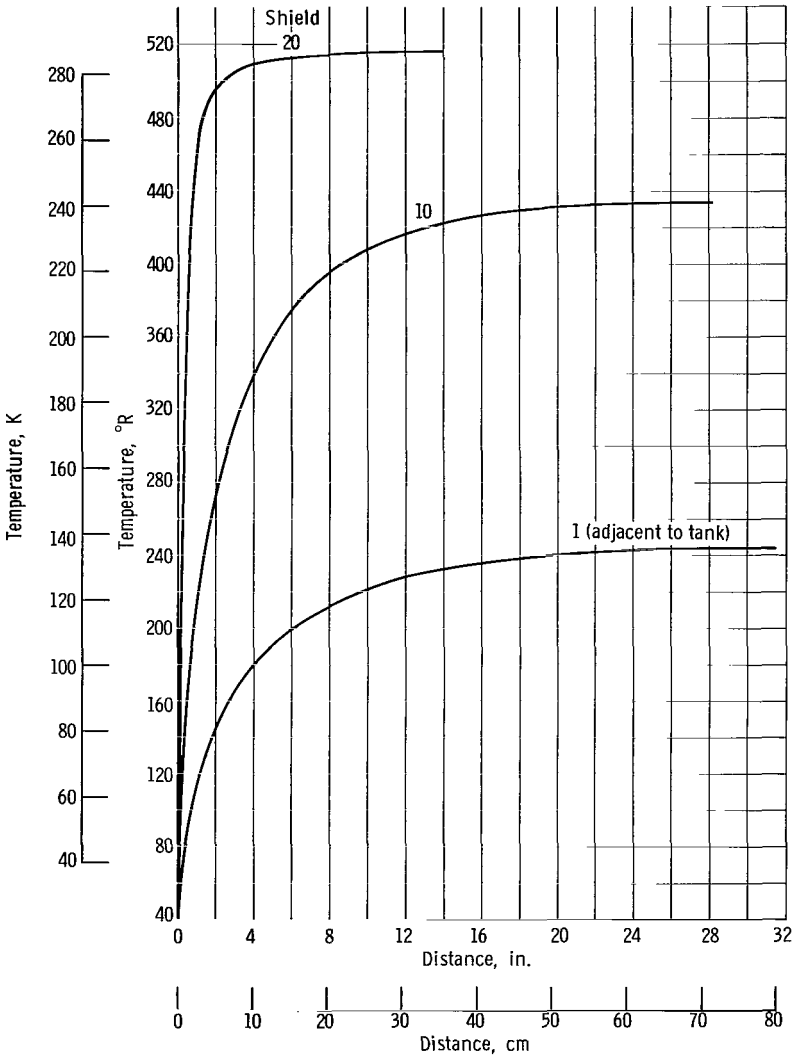

Figure 6. - Temperature profiles for 1st, 10th, and 20th shields of a 20-shield system thermally shorted to a 2-inch- (5.1-cm-) diameter penetration as function of distance from penetration. Radiating source temperature, T_{rs}, 520° R (289 K); shield thermal conductivity, k_s, experimental; shield emissivity, ϵ_s, 0.024.

in the vicinity of the penetration. The severity of the temperature profile ($\Delta T/\Delta r$ ratio) determined the magnitude of heat conduction along any particular shield into the penetration. This ratio increases for shields farther away from the tank and reaches a maximum for the top shield.

The increasing ratio for shields nearing the top results from two independent effects. First the shields nearing the top are exposed to increasingly higher undisturbed shield temperatures, thus increasing the potential ΔT available. The undisturbed shield temperature is that temperature which exists on the shield when the lateral heat conduction approaches zero. Secondly, the distance required for a given shield to recover to its undisturbed temperature increases for shields nearer the tank wall. This has the effect of increasing the effective heat path. This trend is independent of the number of shields comprising the insulation system as shown in figure 7.

A qualitative explanation of this trend considers a heat balance about the top shield. The total quantity of heat transferred through an area of insulation surrounding a penetration is dependent solely on the temperature profile of the top shield. This profile deter-

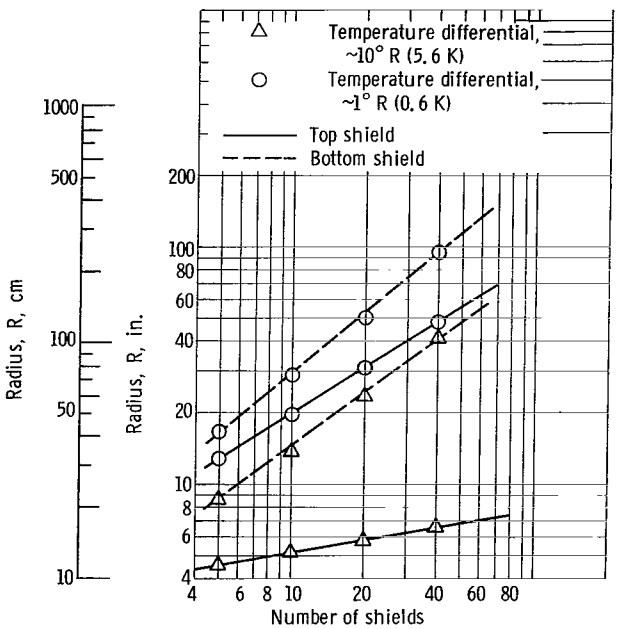

Figure 7. - Radius about a 2-inch- (5.1-cm-) diameter penetration for the top and bottom shields to reach a specific temperature differential from the undisturbed temperature for that shield as function of number of shields in the system. Radiating source temperature, T_{rs}, 520° R (289 K); shield thermal conductivity, k_s, experimental; shield emissivity, ϵ_s, 0.024.

mines the net exchange of radiation between the radiating source and the top shield, as expressed in

$$Q_{norm,\,rad} = \sum_{A} \Delta A \sigma F_{rs,N}\left(T_{rs}^4 - T_{N,r}^4\right)$$

If the conduction term along the top shield were zero, all radiation received by the top shield would necessarily be passed on to the shield below. Considering $F_{rs,N}$ equal to $F_{N,N-1}$ results in the temperature relation

$$\left(T_{rs}^4 - T_{N,r}^4\right) = \left(T_{N,r}^4 - T_{N-1,r}^4\right)$$

Table I illustrates how small changes in $T_{N,r}$ cause significantly larger changes in $T_{N-1,r}$ for a constant radiating source temperature of 520° R (289 K). Thus for temperatures on the top shield less than 437° R (243 K), the shield below could not attain the required temperature to keep the net exchange approximately the same. To compensate for this, the incremental areas on the second shield must be larger than their corresponding areas on the first shield. This same argument can be used to show why the degraded area for any other shield must be less than the degraded area of the shield below it and greater than the degraded area of the shield above it.

TABLE I. - SHIELD TEMPERATURE COMPARISON FOR PURE RADIATION HEAT TRANSFER

[Radiating source temperature, 520° R (289 K).]

Temperature			
$T_{N,r}$		$T_{N-1,r}$	
$^{\circ}$R	K	$^{\circ}$R	K
500	278	477	265
480	268	426	237
460	256	358	199
440	244	207	115
437	243	69	38

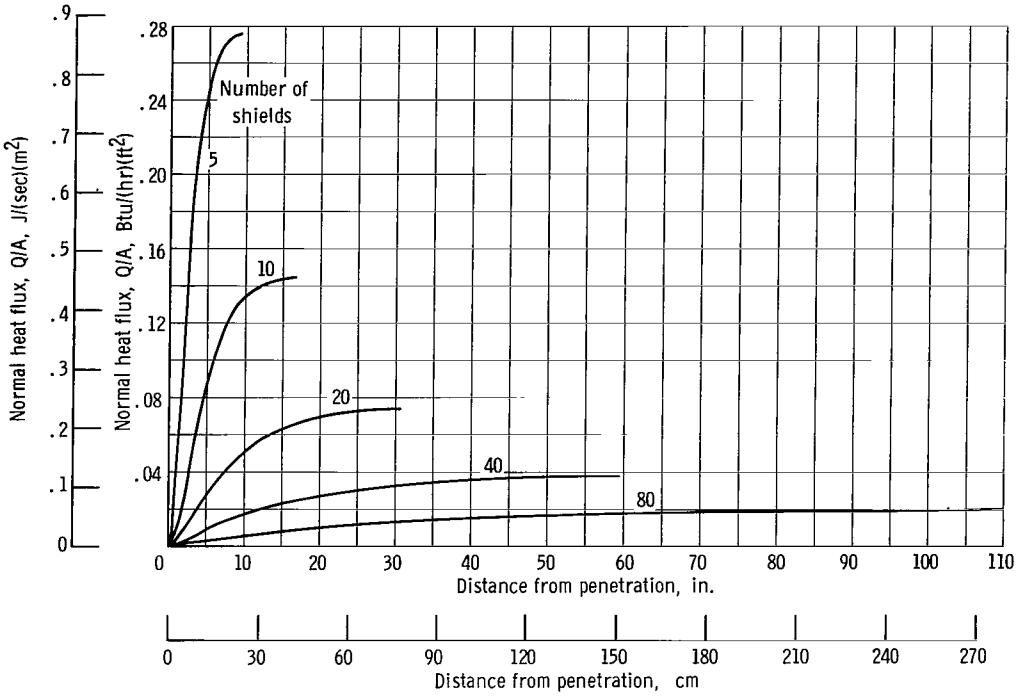

Figure 8. - Normal heat flux as function of distances from a 2-inch- (5.1-cm-) diameter penetration for various number of shields. Radiating source temperature, T_{rs}, 520° R (289 K); shield thermal conductivity, k_s, experimental; shield emissivity, ϵ_s, 0.024.

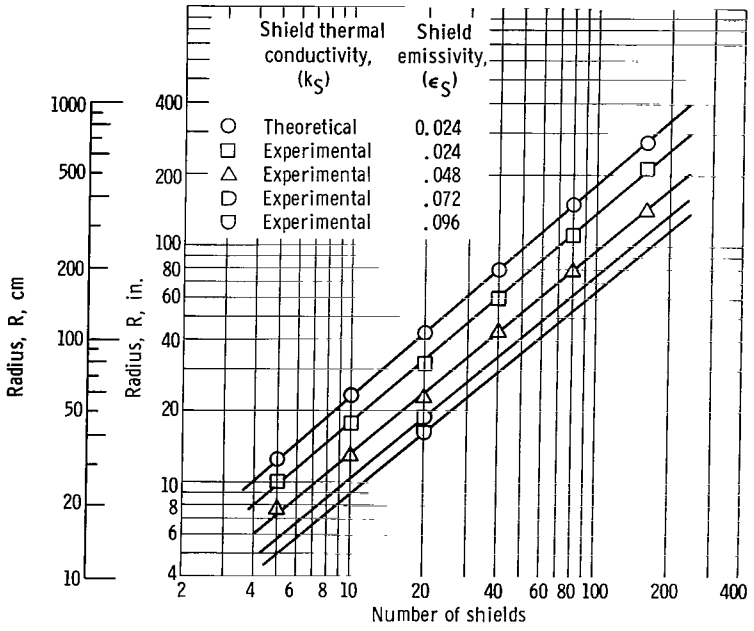

Figure 9. - Radius of thermally degraded area (Q_{norm} = 0.99 $Q_{norm, und}$) around 2-inch- (5.1-cm-) diameter penetration as function of number of shields. Radiating source temperature, T_{rs}, 520° R (289 K).

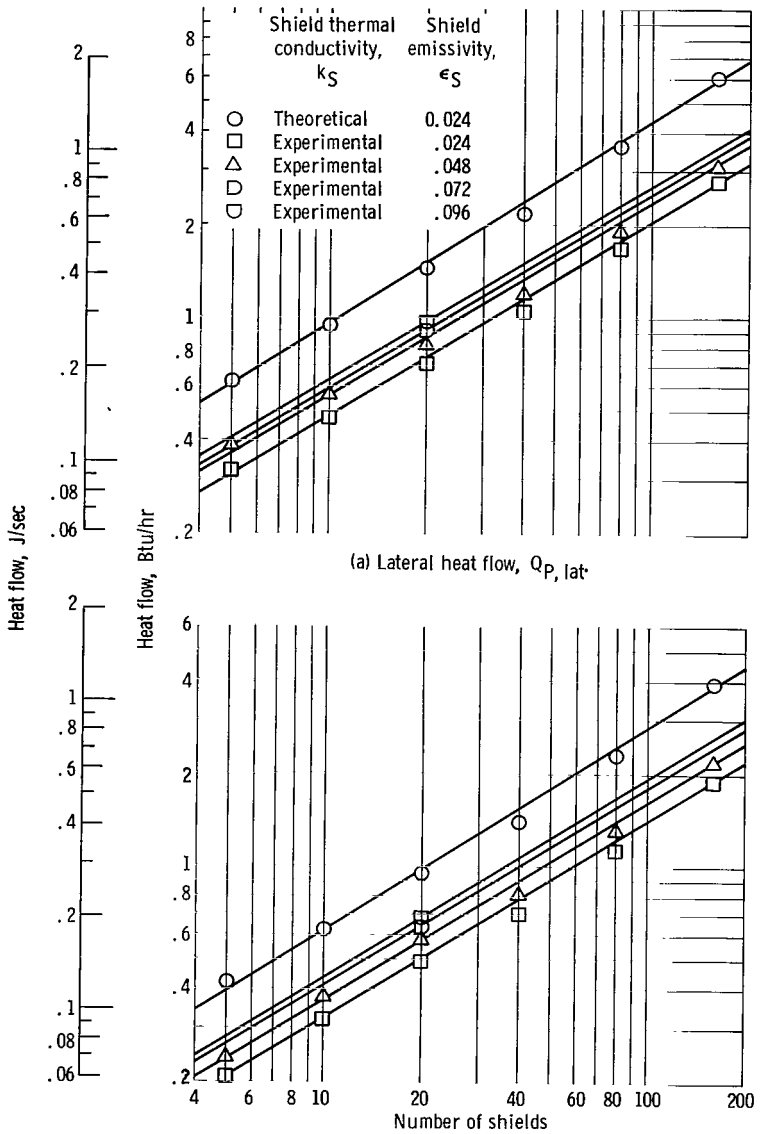

(a) Lateral heat flow, $Q_{P, lat}$.

(b) Net increase in heat flow, ΔQ_p.

Figure 10. - Heat flow into tank for a 2-inch- (5.1-cm-) diameter penetration as function of number of shields. Radiating source temperature, T_{rs}, 520° R (289 K).

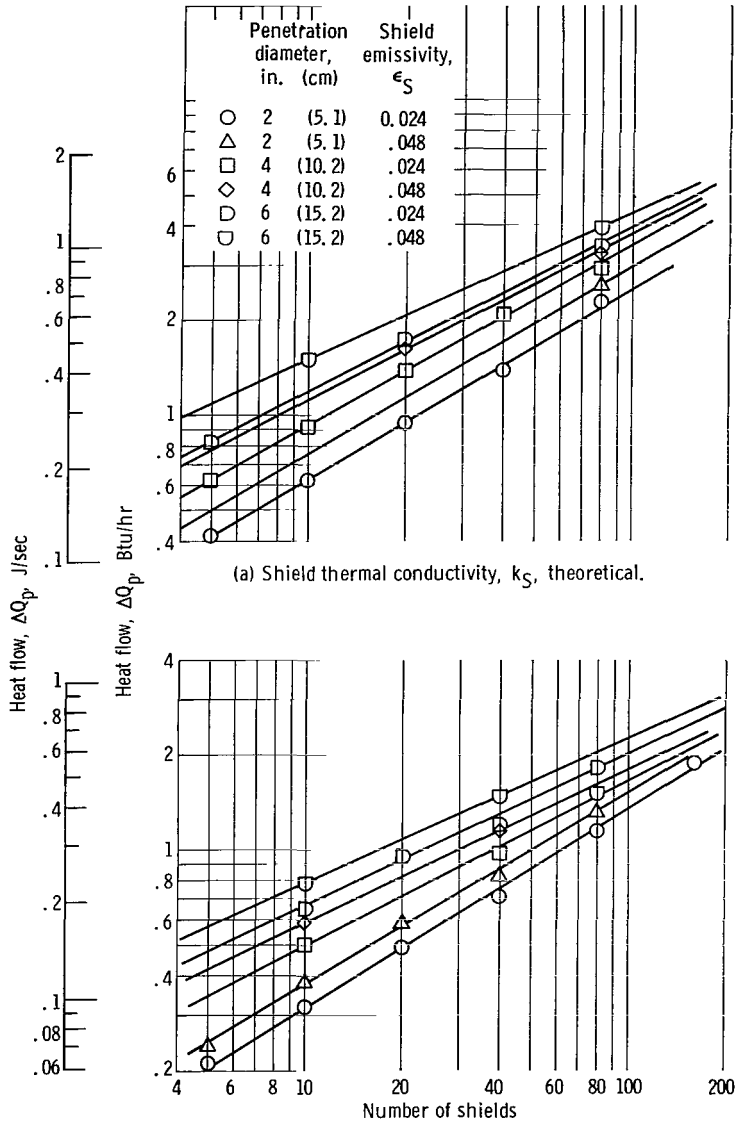

(a) Shield thermal conductivity, k_S, theoretical.

(b) Shield thermal conductivity, k_S, experimental.

Figure 11. - Net increase in heat flow into tank for various diameter penetrations as function of number of shields. Radiating source temperature, T_{rs}, 520° R (289 K).

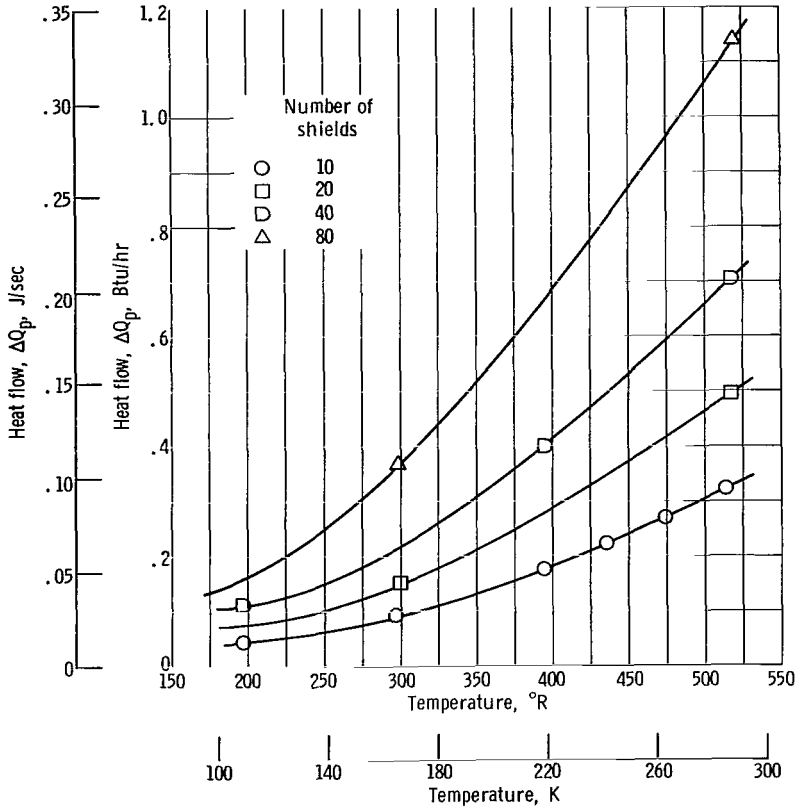

Figure 12. - Net increase in heat flow into tank for 2-inch- (5.1-cm-) diameter penetration as function of undisturbed top shield temperature. Shield thermal conductivity, k_S, experimental; shield emissivity, ϵ_S, 0.024.

The degraded temperatures on the shield adjacent to the tank decrease the normal radiation from this shield to the tank as shown in figure 8. The end point on each curve represents the arbitrarily defined disturbed radius where the normal radiation component equals 0.99 of the undisturbed heat flux. The disturbed radius sets the degraded area used for determining the net heat flow into the tank.

The radii defining the thermally degraded area for various number of shields for two different shield thermal conductivities and for various shield emissivities are shown in figure 9. In general, doubling the number of shields tends to double the radius of the thermally degraded area for any set of variables. As the shield emissivity increases, the radius decreases. Changing the normal component by radiation does not significantly change the heat conducted laterally along the shield. Thus, any particular shield does not have to draw on as large an area to essentially transfer the same amount of heat to the penetration.

The direct lateral heat flow to the penetration $Q_{p,lat}$ and the net increase in heat flow into the tank ΔQ_p as a function of the number of shields and shield emissivities are

shown in figures 10(a) and (b), respectively. In general, doubling the number of shields increases the respective heat flows by approximately 50 percent. Doubling the number of shields doubles the effective number of individual heat paths. However, this potential increase is partially offset by the fact that doubling the number of shields also increases the effective heat path for any given shield (i.e., the disturbed radius increases). For any given set of conditions ΔQ_p is approximately equal to 0.67 $Q_{p,\,lat}$.

The effect of various diameter penetrations on ΔQ_p as a function of the number of shields for both the theoretical and experimental values of shield thermal conductivity is shown in figure 11. Increasing the penetration diameter has less effect on ΔQ_p on a percentage basis as the number of shields is increased (i.e., the curves converge). This trend indicates that for the low number of shields the shield cross-sectional area is more influential than the number of individual heat paths in determining the lateral heat flows. For the high number of shields the reverse is true.

The effect of changing the undisturbed top shield temperature on the net heat flow into the tank (ΔQ_p) is shown in figure 12. Various top shield temperatures are obtained by exposing the shield to different radiating source temperatures. Since radiation heat transfer is proportional to the fourth power of the temperature, the curves in figure 12 are not linear. The data from figure 12 are normalized in figure 13 to a reference temperature of 520° R (289 K). The normalized curve is independent of the number of shields being used.

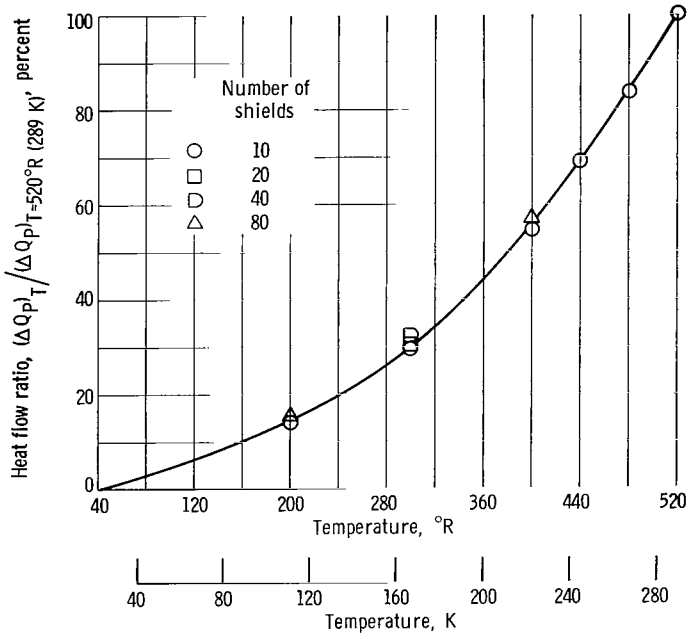

Figure 13. - Ratio of net increase in heat flow into tank for a given undisturbed top shield temperature to that heat flow when this shield temperature is 520° R (289 K). Shield thermal conductivity, k_S, experimental; shield emissivity, ϵ_S, 0.024.

Case 2 - Thermal Contact Resistance for Shield Penetration Model

All of the data presented in Case 1 assumed a perfect thermal short between each shield edge and the penetration. An actual application would offer some finite thermal contact resistance (TCR) even if the installation were perfect (i.e., no gap between the shield edge and the penetration).

The value of TCR as previously defined in the analysis decreases the lateral heat flow along each shield by specifying the shield edge temperature $T_{p,i}$:

$$TCR = 100 \frac{T_{p,i} - T_{lh}}{T_{und,i} - T_{lh}}$$

The shield edge temperature profiles for various values of TCR for a 20-shield insulation system are shown in figure 14. Curves of this type can be used to determine a range

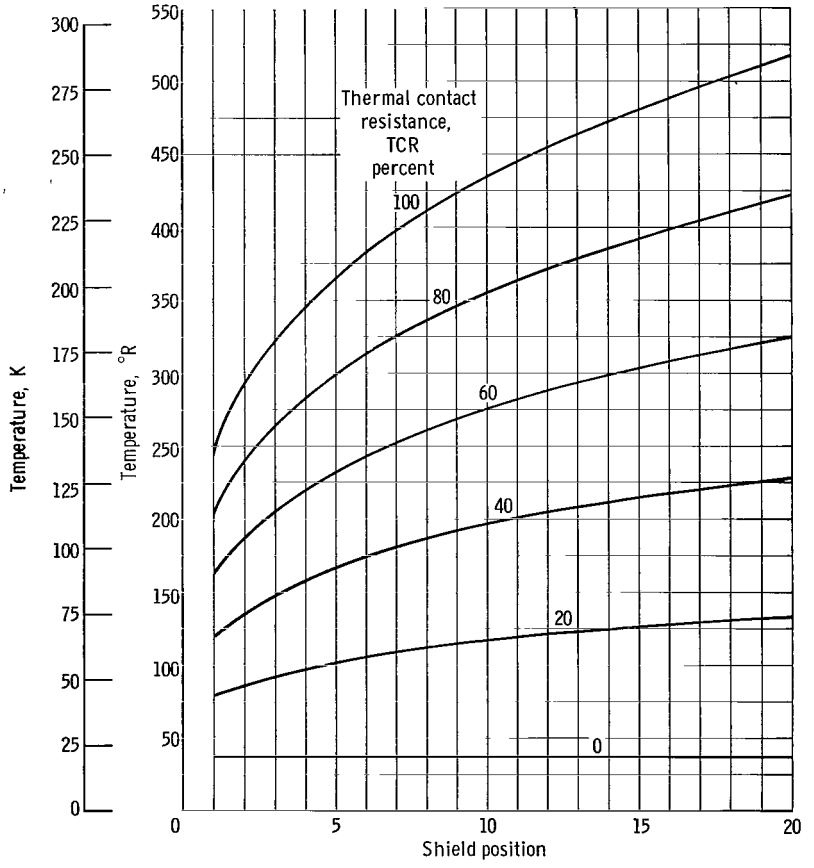

Figure 14. - Shield edge temperature profiles for a 20-shield system as function of thermal contact resistance.

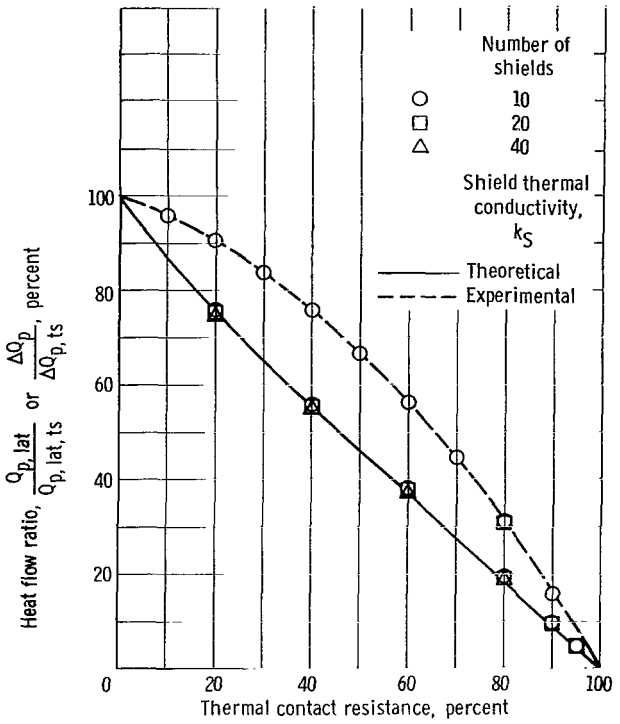

Figure 15. - Ratio of direct lateral heat flow to a penetration and/or net increase in heat flow into the tank to its respective thermally shorted value as function of thermal contact resistance.

of values of TCR to use in terms of an anticipated temperature difference between a given shield and the penetration. Specific values of thermal contact resistance to use will have to await experimental testing. Quite possibly the installation technique and care in handling will greatly influence the value of TCR to be determined.

The ratios of $Q_{p,lat}$ and/or ΔQ_p to their respective thermally shorted values as a function of TCR are shown in figure 15. The ratios are independent of the number of shields, but highly dependent on the thermal conductivity of the shield. This is due to the fact that the experimental value of thermal conductivity decreases with lower temperatures, while the theoretical value does the opposite.

Case 3 - Use of Thermal Buffer Zone Between Shields and Penetration

The data presented in this section consider the shields thermally shorted to the buffer zone. The buffer zone in turn is thermally shorted to the penetration and tank. All tem-

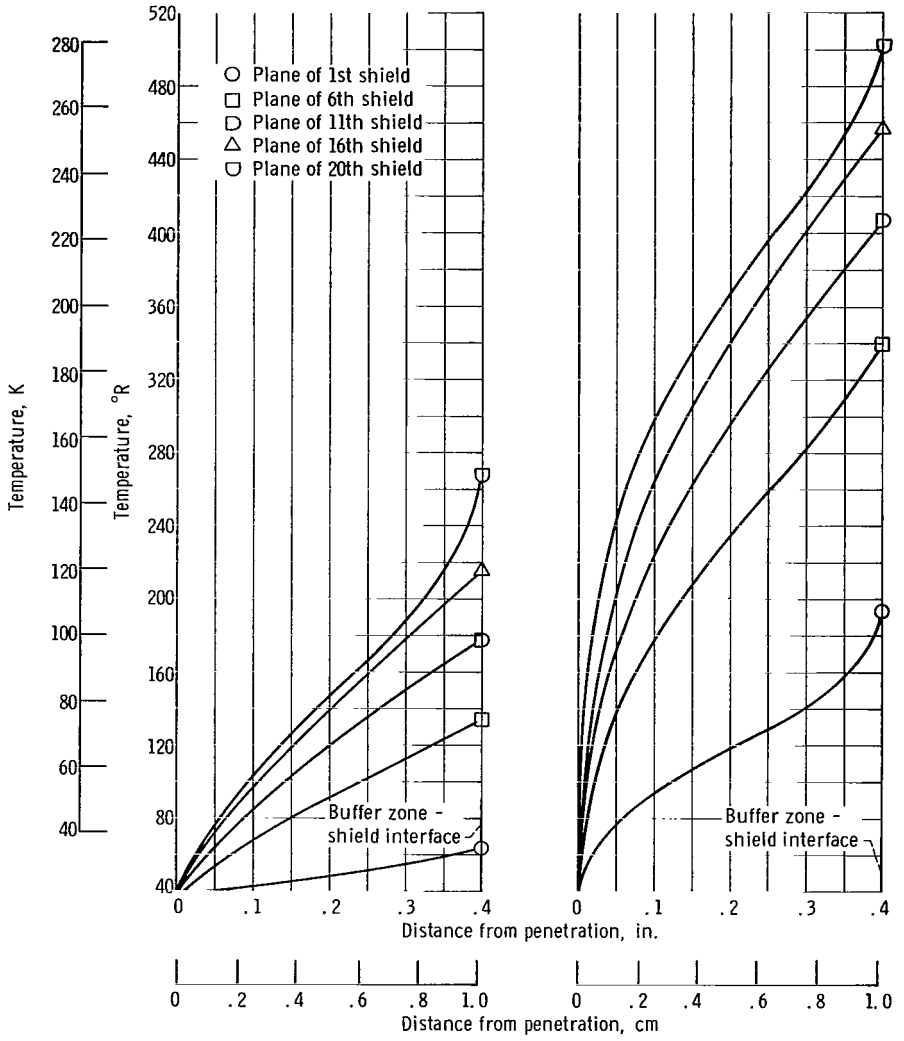

(a) Average buffer zone thermal conductivity, $k_{B, avg}$, 0.0095 Btu per foot per hour per °R (0.0164 J/(m)(sec)(K)).

(b) Average buffer zone thermal conductivity, $k_{B, avg}$, 0.0004 Btu per foot per hour per °R (0.00069 J/(m)(sec)(K)).

Figure 16. - Temperature profile through a 0.4-inch-(1-cm-) square buffer zone thermally shorted to a 20-shield system. Radiating source temperature, T_{rs}, 520° R (289 K); shield thermal conductivity, k_S, experimental; shield emissivity, ϵ_S, 0.024.

peratures on the tank surface and penetration are set at 37° R (20.6 K). Unless specified otherwise, the following values for the variables are used:

Shield emissivity, ϵ_S 0.024
Penetration diameter, D_p, in. (cm) 2 (5.1)
Shield spacing, Δz_S, in. (cm) 0.020 (0.051)
Shield thermal conductivity, k_S . . . . . experimental
Radiating source temperature, T_{rs}, $^{\circ}$R (K) 520 (289)

The temperature profiles through the buffer zone corresponding to the planes of the 1st, 6th, 11th, 16th, and 20th shields of a 20-shield system are shown in figure 16. The two average thermal conductivities $k_{B,avg}$ of the buffer zone material (0.0095 and 0.0004 Btu/(ft)(hr)($^{\circ}$R); 0.0164 and 0.00069 J/(m)(sec)(K)) represent the extremes for appropriate insulation materials. In each case the buffer zone width was arbitrarily set equal to the buffer zone height of 0.40 inch (1.02 cm).

As would be expected, the lower $k_{B,avg}$ yields the higher temperature profile at the shield - buffer zone interface. As the temperature profile at this interface increases, the quantity of heat transferred laterally from the shields to the buffer zone must decrease. The optimum profile at this interface would be the undisturbed temperatures of the individual shields.

The effect of the buffer zone width and thermal conductivity on the heat transferred through the buffer zone for a 20-shield system is shown in figure 17. The two buffer zone heights of 0.20 and 0.40 inch (0.51 and 1.02 cm) represent shield spacings of 0.010 and 0.020 inch (0.025 and 0.051 cm), respectively. In each configuration, increasing the buffer width decreased the lateral heat flow into the penetration ($Q_{B,lat}$), but increased the normal heat flow into the tank ($Q_{B,norm}$). The optimum geometric configuration is that configuration which minimizes the total heat flow into the tank ($Q_{B,lat} + Q_{B,norm}$).

This minimum heat flow occurred at a buffer width approximately equal to the buffer height, and at a width three-fourths of the height for $k_{B,avg}$ = 0.0004 Btu per foot per hour per $^{\circ}$R (0.00069 J/(m)(sec)(K)). For $k_{B,avg}$ = 0.0095 Btu per foot per hour per $^{\circ}$R (0.0164 J/(m)(sec)(K)), this minimum heat flow occurred at a buffer width varying from one-half to three-fourths of the buffer height. However, the net increase in heat flow into the tank for a buffer material having $k_{B,avg}$ = 0.0095 Btu per foot per hour per $^{\circ}$R (0.0164 J/(m)(sec)(K)) was approximately that obtained without a buffer zone. (This is discussed in more detail in conjunction with fig. 20.) All new data presented will approximate optimum values for acceptable buffer zone materials by using a square configuration.

Using a shield spacing of 0.010 or 0.020 inch (0.025 and 0.051 cm) ($B_w = B_h$ = 0.2 and 0.4 in. (0.51 and 1.02 cm), respectively, for a 20-shield system) has very little ef-

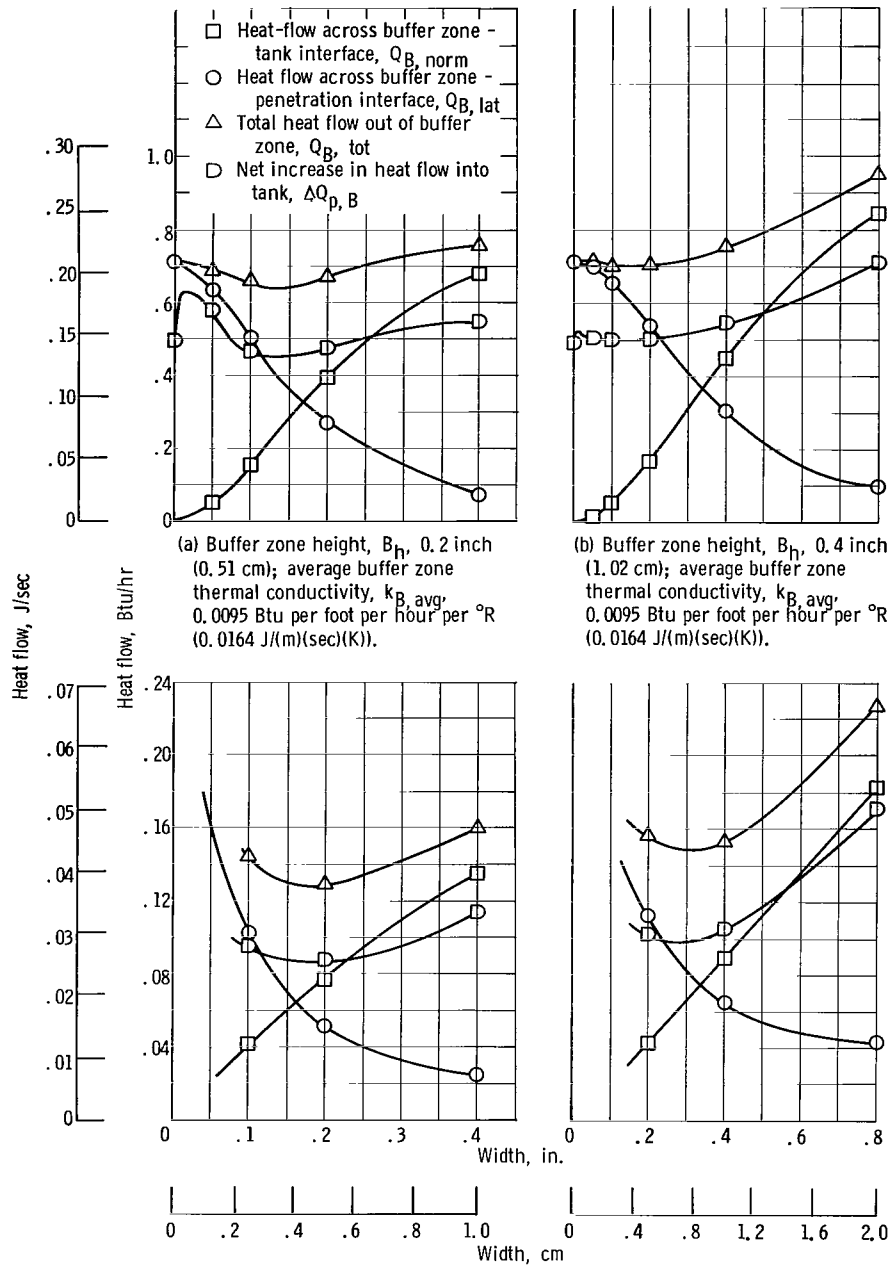

(a) Buffer zone height, B_h, 0.2 inch (0.51 cm); average buffer zone thermal conductivity, $k_{B, avg}$, 0.0095 Btu per foot per hour per °R (0.0164 J/(m)(sec)(K)).

(b) Buffer zone height, B_h, 0.4 inch (1.02 cm); average buffer zone thermal conductivity, $k_{B, avg}$, 0.0095 Btu per foot per hour per °R (0.0164 J/(m)(sec)(K)).

(c) Buffer zone height, B_h, 0.2 inch (0.51 cm); average buffer zone thermal conductivity, $k_{B, avg}$, 0.0004 Btu per foot per hour per °R (0.00069 J/(m)(sec)(K)).

(d) Buffer zone height, B_h, 0.4 inch (1.02 cm); average buffer zone thermal conductivity, $k_{B, avg}$, 0.0004 Btu per foot per hour per °R (0.00069 J/(m)(sec)(K)).

Figure 17. - Effect of buffer zone width on heat flows through a buffer zone thermally shorted to a 2-inch- (5.08-cm-) diameter penetration and a 20-shield system. Radiating source temperature, T_{rs}, 520° R (289 K); shield emissivity, ϵ_S, 0.024; shield thermal conductivity, k_S, experimental.

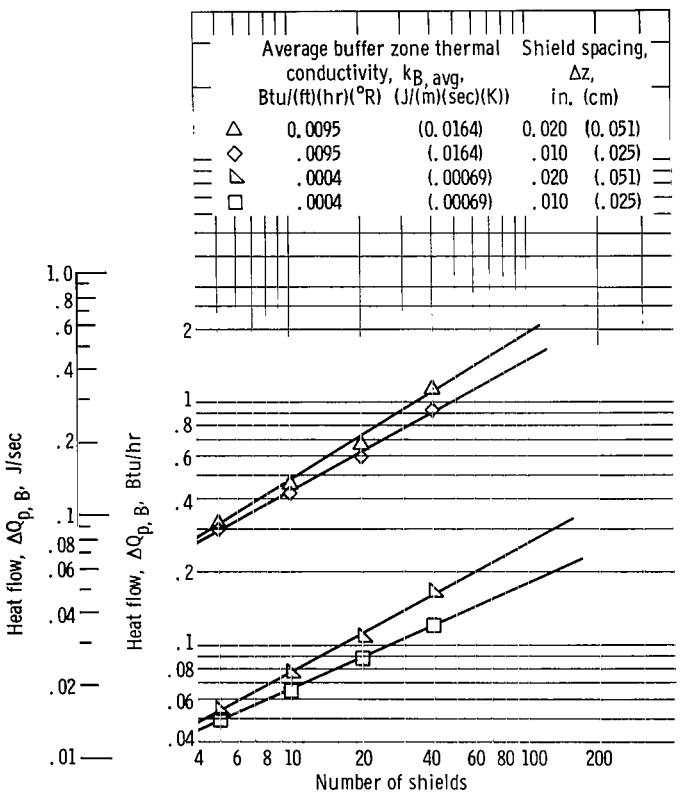

Figure 18. - Effect of shield spacing on net increase in heat flow into tank as function of number of shields. Radiating source temperature, T_{rs}, 520° R (289 K); shield emissivity, ϵ_S 0.024; shield thermal conductivity, k_S, theoretical; penetration diameter, D_p, 2 inches (5.1 cm).

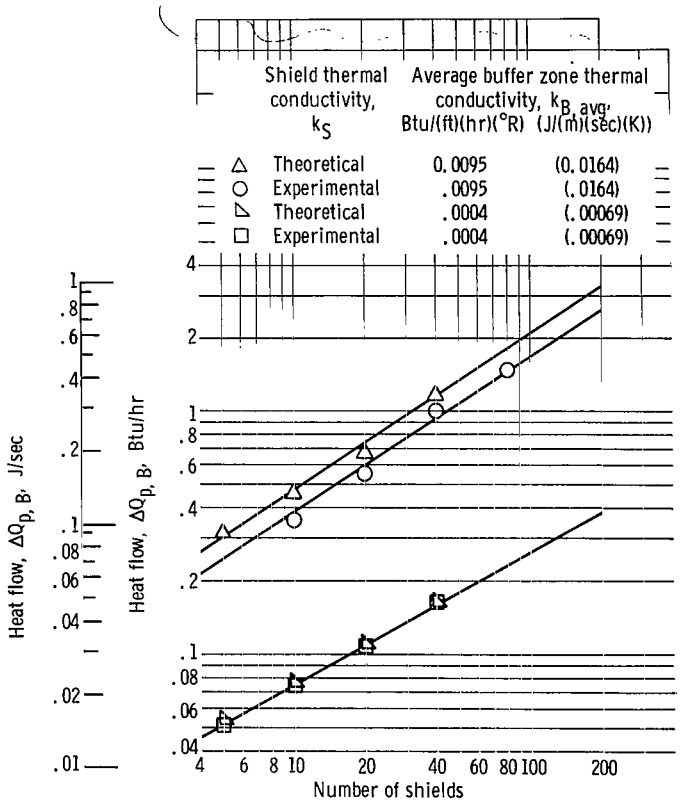

Figure 19. - Effect of shield thermal conductivity on net increase in heat flow into the tank as function of number of shields. Radiating source temperature, T_{rs}, 520° R (289 K); shield emissivity, ϵ_S, 0.024; shield spacing, Δz, 0.020 inch (0.051 cm); penetration diameter, D_p, 2 inches (5.1 cm).

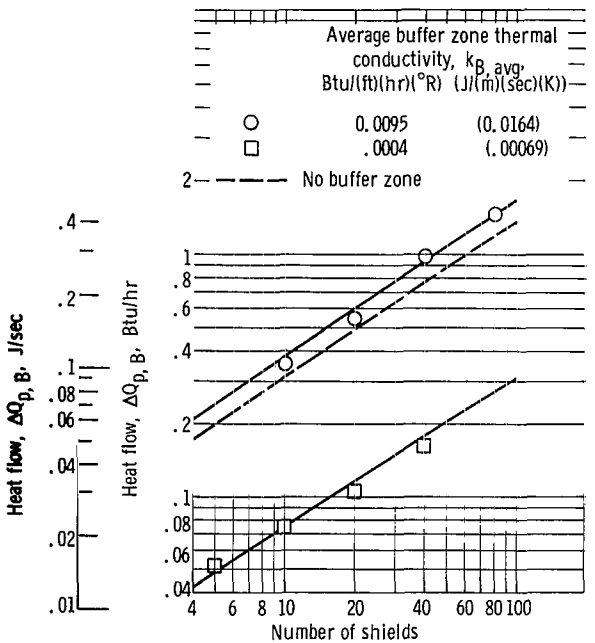

Figure 20. - Net increase in heat flow into the tank with or without a buffer zone as function of number of shields. Radiating source temperature, T_{rs}, 520° R (289 K); shield emissivity, ϵ_S, 0.024; shield thermal conductivity, k_S, experimental; shield spacing, Δz, 0.020 inch (0.051 cm); penetration diameter, D_p, 2 inches (5.1 cm).

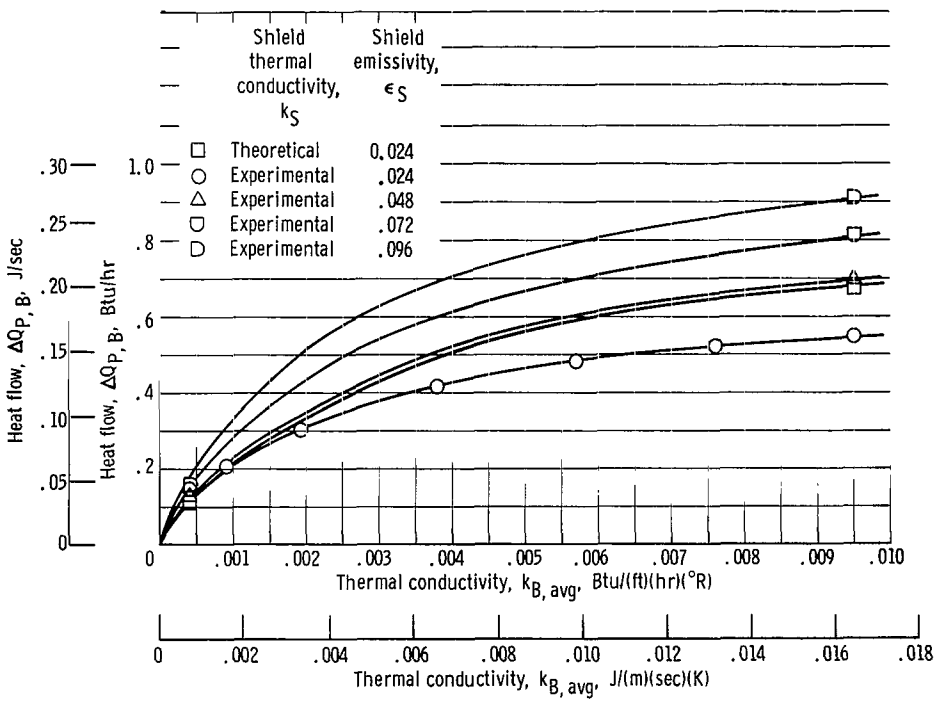

Figure 21. - Net increase in heat flow into the tank as function of average thermal conductivity of buffer zone. Number of shields, 20; radiating source temperature, T_{rs}, 520° R (289 K); shield spacing, Δz, 0.020 inch (0.051 cm); penetration diameter, D_p, 2 inches (5.1 cm).

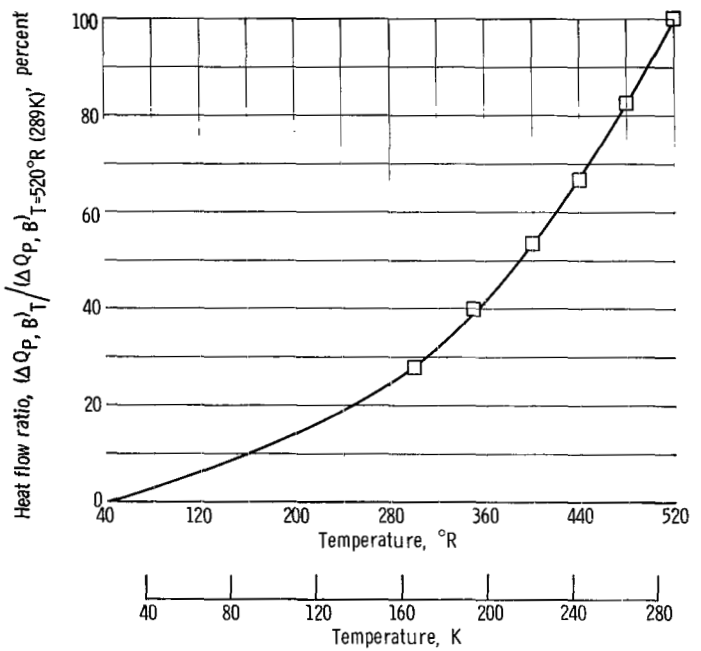

Figure 22. - Ratio of net increase in heat flow into the tank for a given undisturbed top shield temperature to heat flow when this shield temperature is 520° R (289 K). Number of shields, 20; shield thermal conductivity, k_S, experimental; shield emissivity, ϵ_S, 0.024; average buffer zone thermal conductivity, $k_{B,avg}$, 0.0095 Btu per foot per hour per °R (0.0164 J/(m)(sec)(K)).

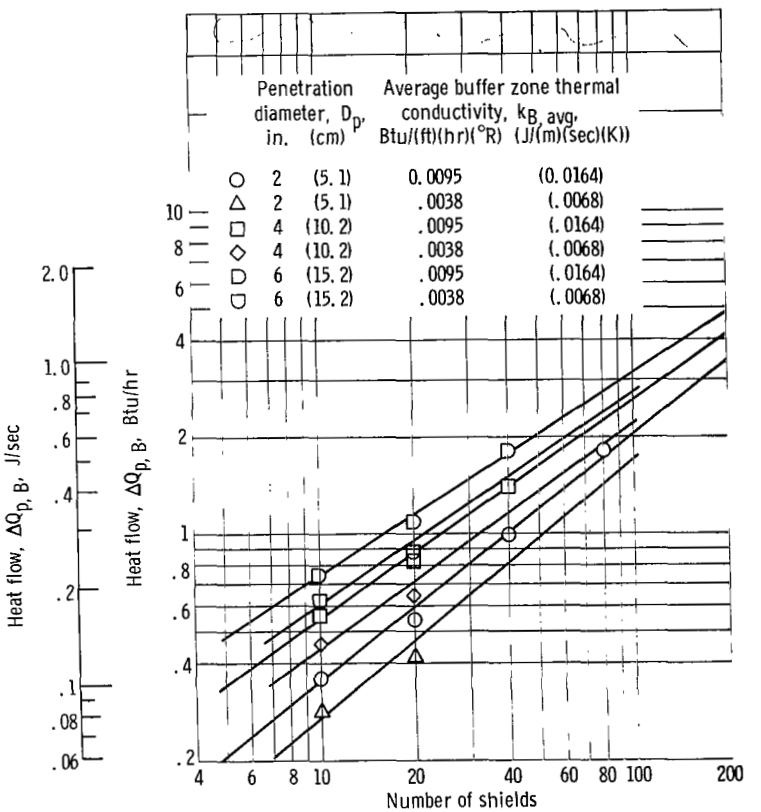

Figure 23. - Net increase in heat flow into the tank using a buffer zone around various diameter penetrations as function of number of shields. Radiating source temperature, T_{rs}, 520° R (289 K); shield thermal conductivity, k_S, experimental shield emissivity, ϵ_S, 0.024.

fect on $\Delta Q_{p,B}$. This is shown in figure 18 for $k_{B,avg}$ = 0.0095 and 0.0004 Btu per foot per hour per ^{o}R (0.0164 and 0.00069 J/(m)(sec)(K)) and the theoretical value of k_S. The significant change in ΔQ_p occurs with changes in $k_{B,avg}$ for a given number of shields.

The effect of shield thermal conductivity on $\Delta Q_{p,B}$ becomes less significant as $k_{B,avg}$ decreases. As shown in figure 19, the use of either experimental or theoretical results in the same $\Delta Q_{p,B}$ when $k_{B,avg}$ = 0.0004 Btu per foot per hour per ^{o}R (0.00069 J/(m)(sec)(K)).

Doubling the number of shields increases the $\Delta Q_{p,B}$ by approximately 50 percent for both values of $k_{B,avg}$ as shown in figure 20. This relation is exactly the same as was previously shown for the shields butted directly to the penetration. The comparable data from figure 10(b) for the shield-penetration configuration are replotted in figure 20. This curve indicates that use of a buffer zone for $k_{B,avg}$ = 0.0095 Btu per foot per hour per ^{o}R (0.0164 J/(m)(sec)(K)) is thermally inferior to the no-buffer zone configuration. For buffer zone thermal conductivities in this range, the decreased lateral heat flow was offset by the increased normal heat flow through the buffer zone. Since all known conventional buffer zone materials are isotropic, the analysis considered the thermal conductivity equal in both the lateral and normal directions. Thus, a reduction of the lateral heat flow could be accomplished only by an increase in the normal heat flow. As shown, there is a limiting value of thermal conductivity that a buffer zone can have to still warrant its use.

The effect changing $k_{B,avg}$ has on $\Delta Q_{p,B}$ for various shield emissivities is shown in figure 21. The value of ϵ_S used becomes insignificant only at low values of $k_{B,avg}$. At the higher values of $k_{B,avg}$, the increase in ϵ_S creates a higher potential quantity of heat to be transferred laterally into the buffer zone.

The ratio of $\Delta Q_{p,B}$ for a given undisturbed top shield temperature to the $\Delta Q_{p,B}$ when this top shield temperature is 520^{o} R (289 K) is shown in figure 22. Again the curve is nonlinear since radiation heat exchange is proportional to the fourth power of the temperature.

The effect of changing the penetration diameter on $\Delta Q_{p,B}$ is shown in figure 23. As shown previously for the shield-penetration model, the curves again tend to converge at the high number of shields.

Case 4 - Thermal Contact Resistance for the Buffer Zone

All of the results presented for Case 3 assume that the buffer zone is thermally shorted to the edges of the shields as well as to the penetration and tank surface. This results in maximum heat flows through the buffer zone, and thus eventually into the tank. To adjust these results for an actual application, a correction factor expressing thermal contact resistance has been generated.

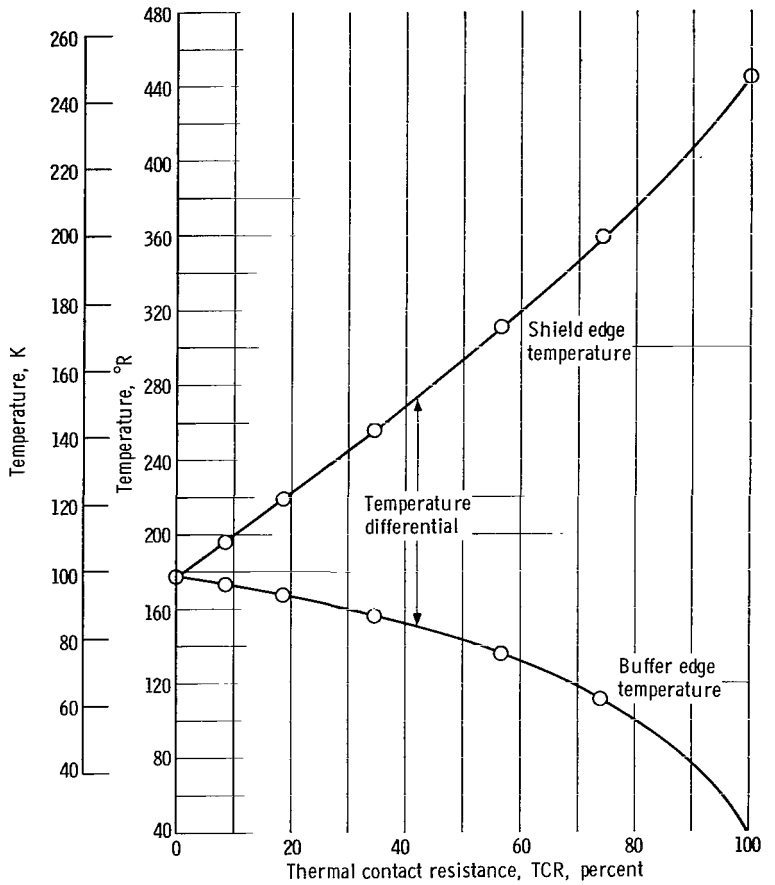

Figure 24. - Temperature differential across buffer zone - shield junction in plane of 11th shield of 20-shield system as function of thermal contact resistance.

Thermal contact resistance has been considered at the buffer zone - shield interface only. This means that any decreased heat flow through the buffer zone will be realized by reducing the lateral heat flow across this interface. This is valid since the data show that approximately 90 percent of the total heat flow through the buffer zone does in effect cross this interface. The other 10 percent is by direct radiation received by the top surface of the buffer zone.

The resulting ΔT at the buffer-shield interface to simulate various values of thermal contact resistance is shown in figure 24. At TCR = 0, a thermal short exists; and for TCR = 100 percent, the shield edge temperature is the undisturbed temperature for that shield. Experimental measurements of the existing ΔT across the interface will enable calculation of a range of actual TCR values to use in future analyses.

The ratio of $\Delta Q_{p,B}$ to its thermally shorted value as a function of TCR is shown in figure 25. Various values of $k_{B,avg}$ as well as two different number of shields were used to generate the data. As indicated, the results show a well defined relation.

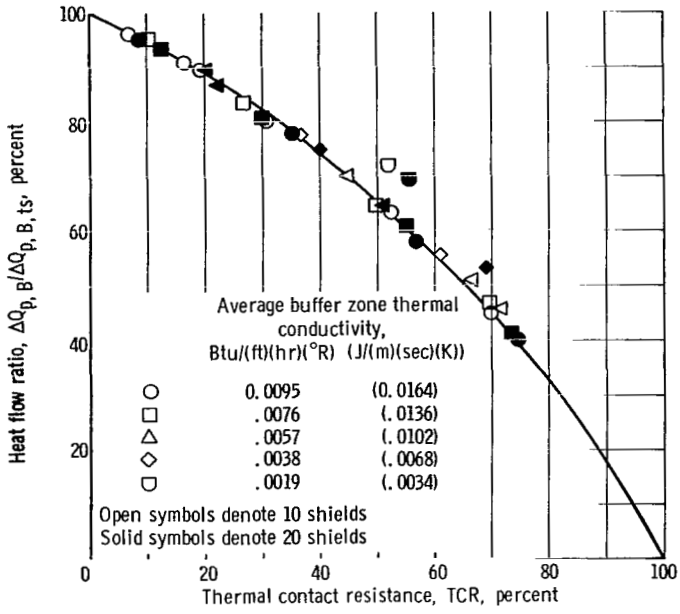

Figure 25. - Ratio of net increase in heat flow into the tank for a given buffer zone configuration to its respective thermally shorted value as function of thermal contact resistance. Shield thermal conductivity, k_S, experimental.

General Comparisons and Conclusions

The data presented in the preceding four cases can be used to estimate the degree of thermal degradation attributed to several representative penetration configurations. However, these results cannot be clearly presented on a single figure because of the many variables involved. To avoid scanning numerous figures to estimate the performance, curve fits of the data obtained in both Cases 1 and 3 have been made. These curve fits are equations which approximate the effect each variable has on the heat flows and degraded radius. For the case of the shields thermally shorted to the penetration the following are true:

$$Q_{p,\,lat,\,S}\left(\frac{Btu}{hr}\right) = 0.48\left(\frac{N}{10}\right)^{0.58}\left(\frac{\epsilon_S}{0.024}\right)^{0.24}\left(\frac{D_p}{2}\right)^{0.51}\left(\frac{T_{S,N}}{520}\right)^{2.16}$$

$$\Delta Q_{p,S}\left(\frac{Btu}{hr}\right) = 0.32\left(\frac{N}{10}\right)^{0.59}\left(\frac{\epsilon_S}{0.024}\right)^{0.26}\left(\frac{D_p}{2}\right)^{0.54}\left(\frac{T_{S,N}}{520}\right)^{2.06}$$

$$R_{dist,S}(\text{in.}) = 18.2\left(\frac{N}{10}\right)^{0.87}\left(\frac{\epsilon_S}{0.024}\right)^{-0.49}\left(\frac{D_p}{2}\right)^{0.10}\left(\frac{T_{S,N}}{520}\right)^{-0.78}$$

For the configuration of the buffer zone between the shields and the penetration the following equations are true:

$$Q_{p,tot,B}\left(\frac{\text{Btu}}{\text{hr}}\right) = 0.49\left(\frac{N}{10}\right)^{0.67}\left(\frac{\epsilon_S}{0.024}\right)^{0.18}\left(\frac{D_p}{2}\right)^{0.70}\left(\frac{T_{S,N}}{520}\right)^{2.38}\left(\frac{k_{B,avg}}{0.0095}\right)^{0.45}$$

$$\Delta Q_{p,B}\left(\frac{\text{Btu}}{\text{hr}}\right) = 0.33\left(\frac{N}{10}\right)^{0.75}\left(\frac{\epsilon_S}{0.024}\right)^{0.22}\left(\frac{D_p}{2}\right)^{0.74}\left(\frac{T_{S,N}}{520}\right)^{2.42}\left(\frac{k_{B,avg}}{0.0095}\right)^{0.47}$$

$$R_{dist,B}(\text{in.}) = 18.05\left(\frac{N}{10}\right)^{0.82}\left(\frac{\epsilon_S}{0.024}\right)^{-0.50}\left(\frac{D_p}{2}\right)^{0.15}\left(\frac{T_{S,N}}{520}\right)^{-0.98}\left(\frac{k_{B,avg}}{0.0095}\right)^{0.11}$$

where D_p is expressed in inches, $T_{S,N}$ in ^{o}R, and $k_{B,avg}$ in Btu per foot per hour per ^{o}R.

The net increase in heat flow into the tank is approximately two-thirds of the direct lateral heat flow to the tank and/or penetration in either configuration. The heat flows are extremely temperature dependent and least affected by changes in emissivity. The disturbed radius in each configuration increases when either the emissivity or radiating source temperature decrease.

The previous relations used the experimental values of the lateral thermal conductivity of the shield against temperature (ref. 3). The shield simulated a 1/4-mil (0.00064-cm) polyester film aluminized on each side to a thickness of 600 Å; thus, the lateral heat conduction path was minimized. The results in graphical form in the body of the report use a theoretical value of thermal conductivity as well. The theoretical value is obtained by using the bulk properties of aluminum, and quite possibly does not apply to thin films. Therefore, the results using the theoretical value may in reality apply to a much thicker coating, and thus may only serve to indicate the magnitude of differences for various coating thicknesses.

The maximum thermal conductivity that a buffer zone material may have and still be thermally competitive with the no-buffer zone configuration can be determined by equating the previous expressions for $\Delta Q_{p,S}$ and $\Delta Q_{p,B}$. Table II lists the wide range of maximum values of $k_{B,avg}$ that the buffer zone may have.

The validity of these comparisons may depend on the experimental value of thermal contact resistance for an actual application. Because of this and other factors, as well

TABLE II. - BUFFER ZONE THERMAL CONDUCTIVITIES GIVING SAME THERMAL PERFORMANCE AS THEIR CORRESPONDING NO-BUFFER ZONE CONFIGURATION

Number of shields, N	Shield emissivity, ϵ_S	Penetration diameter, D_p		Temperature, $T_{S,N}$		Average thermal conductivity of buffer zone material, $k_{B,avg}$	
		in.	cm	^oR	K	Btu/(ft)(hr)(^oR)	J/(m)(sec)(K)
20	0.024	2	5.1	520	289	0.0076	0.0131
80	.024	2	5.1	520	289	.0054	.0093
20	.072	2	5.1	520	289	.0082	.0142
80	.072	2	5.1	520	289	.0058	.0100
20	.024	6	15.3	520	289	.0055	.0095
80	.024	6	15.3	520	289	.0039	.0067
20	.024	2	5.1	400	222	.0088	.0152
80	.024	2	5.1	400	222	.0063	.0109

as different concepts that are not considered in this analysis, the use of a conventional thermal buffer zone may not necessarily offer the best overall thermal performance. One of these concepts would use an anisotropic buffer zone that has a lower thermal conductivity in the normal than in the lateral direction. Thus, the buffer zone width could be increased (decreasing the lateral heat flow) without offsetting any apparent gain with a high normal heat leak. A potential anisotropic buffer zone would use a separate circular segment of basic multilayer insulation immediately around the penetration. Using a separate segment interrupts the lateral heat path into the penetration, while still utilizing the extremely low thermal conductivity in the normal direction.

The relation between the heat flows and the equivalent area of basic insulation these heat flows represent is shown in figure 26. Thus, the heat flows obtained with the previous expressions, either corrected for thermal contact resistance or not, can be related to the performance of the overall insulation system. The areas represent maximum values since the shield emissivity of 0.024 used in the minimum value that could be anticipated for aluminized polyester film.

The radius of the thermally degraded area, defined by $Q_{norm} = 0.99\, Q_{norm,und}$, obtained with various values of ΔQ_p is shown in figure 27. The aforementioned expressions for the degraded radius are valid only for the thermally shorted cases. Although figure 27 is specifically for the shield penetration model, the results approximate those obtained with the buffer zone configurations.

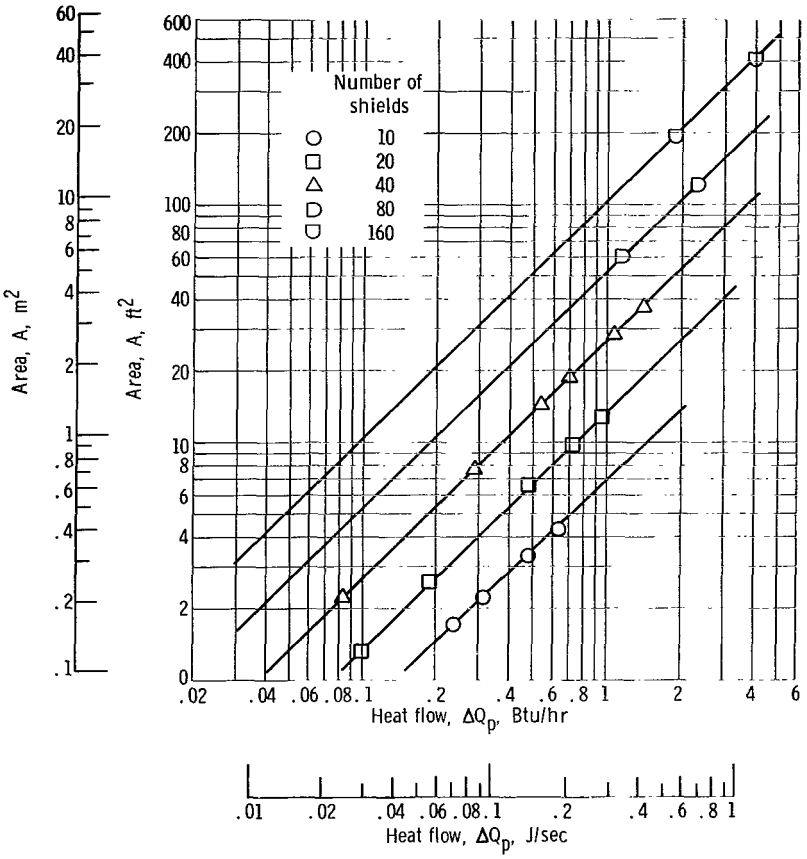

Figure 26. - Net increase in heat flow into the tank expressed as an area of basic insulation transferring the same quantity of heat. Shield emissivity, ϵ_S, 0.024.

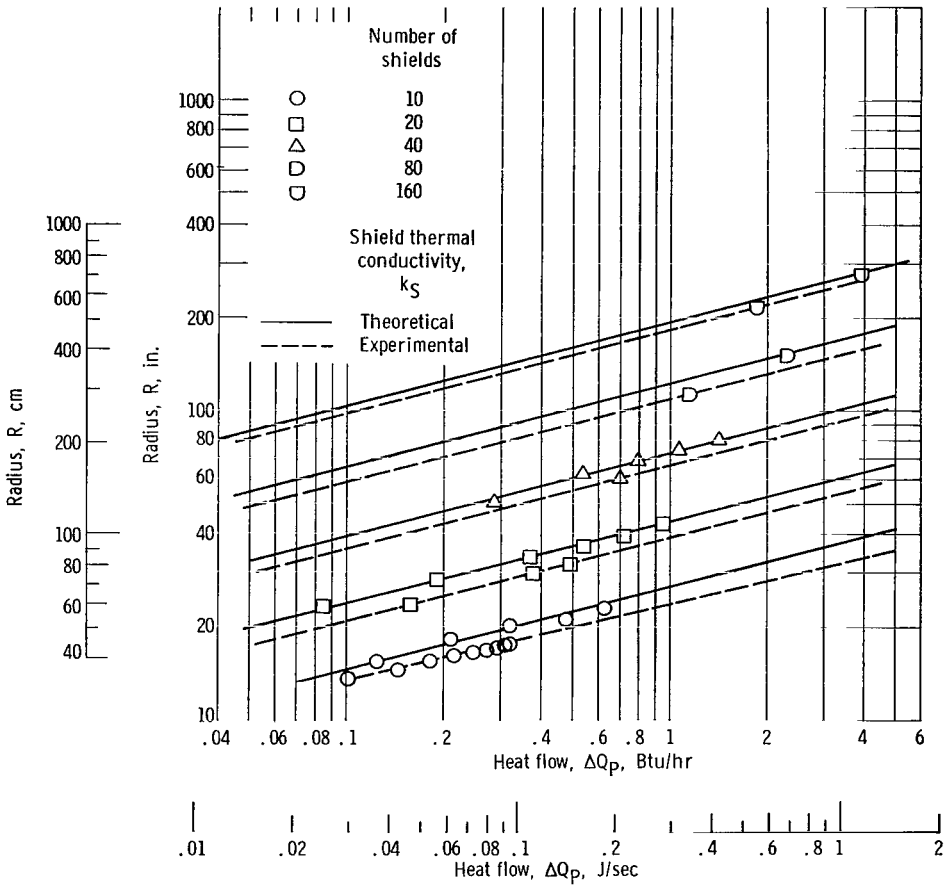

Figure 27. - Radius of thermally degraded area as function of net increase in heat flow into the tank. Shield emissivity, ϵ_S, 0.024.

CONCLUDING REMARKS

An analytical investigation was conducted to determine the direct lateral heat flow to a penetration Q_p, the resultant net increase in heat flow into a tank ΔQ_p, and the radius R_{dist} of the thermally degraded area created by the presence of a cylindrical pipe or tank support penetrating the multilayer insulation on a liquid hydrogen tank. Two different configurations were considered: (1) shield edges butted to the penetration and (2) use of a thermal buffer zone between the shields and the penetration.

The relation between the program variables and the parameters of primary interest can be best expressed in the following equations. These equations represent curve fits of the analytical data. For the configuration of the shields thermally shorted to the penetration the following hold:

$$Q_{p,\,lat,\,S}\left(\frac{Btu}{hr}\right) = 0.48\left(\frac{N}{10}\right)^{0.58}\left(\frac{\epsilon_S}{0.024}\right)^{0.24}\left(\frac{D_p}{2}\right)^{0.51}\left(\frac{T_{S,N}}{520}\right)^{2.16}$$

$$\Delta Q_{p,\,S}\left(\frac{Btu}{hr}\right) = 0.32\left(\frac{N}{10}\right)^{0.59}\left(\frac{\epsilon_S}{0.024}\right)^{0.26}\left(\frac{D_p}{2}\right)^{0.54}\left(\frac{T_{S,N}}{520}\right)^{2.06}$$

$$R_{dist,\,S}(in.) = 18.2\left(\frac{N}{10}\right)^{0.87}\left(\frac{\epsilon_S}{0.024}\right)^{-0.49}\left(\frac{D_p}{2}\right)^{0.10}\left(\frac{T_{S,N}}{520}\right)^{-0.78}$$

where

N number of shields

ϵ_S shield emissivity

D_p penetration diameter, in.

$T_{S,N}$ undisturbed top shield temperature, ^{o}R

The use of a thermal buffer zone between the shields and the penetration yields the following:

$$Q_{p,\,tot,\,B}\left(\frac{Btu}{hr}\right) = 0.49\left(\frac{N}{10}\right)^{0.67}\left(\frac{\epsilon_S}{0.024}\right)^{0.18}\left(\frac{D_p}{2}\right)^{0.70}\left(\frac{T_{S,N}}{520}\right)^{2.38}\left(\frac{k_{B,\,avg}}{0.0095}\right)^{0.45}$$

$$\Delta Q_{p,B}\left(\frac{\text{Btu}}{\text{hr}}\right) = 0.33\left(\frac{N}{10}\right)^{0.75}\left(\frac{\epsilon_S}{0.024}\right)^{0.22}\left(\frac{D_p}{2}\right)^{0.74}\left(\frac{T_{S,N}}{520}\right)^{2.42}\left(\frac{k_{B,avg}}{0.0095}\right)^{0.47}$$

$$R_{dist,B}(\text{in.}) = 18.05\left(\frac{N}{10}\right)^{0.82}\left(\frac{\epsilon_S}{0.024}\right)^{-0.50}\left(\frac{D_p}{2}\right)^{0.15}\left(\frac{T_{S,N}}{520}\right)^{-0.98}\left(\frac{k_{B,avg}}{0.0095}\right)^{0.11}$$

where $k_{B,avg}$ is the average thermal conductivity of the buffer zone material (Btu/(ft)(hr)(^{o}R)).

The previous equations used the experimentally determined values for the lateral thermal conductivity of the shield against temperature (ref. 3). Equating $\Delta Q_{p,S}$ (from the shield-penetration model) to $\Delta Q_{p,B}$ (from the shield-buffer-penetration model) shows that the buffer zone material must have a thermal conductivity, in general, of less than 0.008 Btu per foot per hour per ^{o}R (0.0138 J/(m)(sec)(K)) to warrant its use. Because of thermal contact resistance, as well as the existence or other penetration insulation concepts, the use of a conventional thermal buffer zone may not necessarily offer the best overall thermal performance. An anisotropic buffer zone having a lower thermal conductivity in the normal direction than in the lateral direction may be thermally superior.

The optimum thermal buffer zone configuration (i.e., minimum net heat flow into the tank), in general, has a buffer width approximately three-fourths of the buffer height. This was generally true regardless of the number of shields, spacing of the shields, or the thermal conductivity of the buffer zone material.

To make all of the previous results applicable to a real installation, a correction for possible thermal contact resistance at the shield-penetration interface or shield-buffer zone interface must be made. A definition of thermal contact resistance for both configurations was established. The ratio of ΔQ_p to its thermally shorted value as a function of thermal contact resistance is presented. These correction factors can be applied directly to the equations for $\Delta Q_{p,S}$ and $\Delta Q_{p,B}$ to obtain more representative values of heat flows. Unfortunately exact design values for thermal contact resistance will vary for each insulation configuration and installation technique. A range of values to use will have to be determined by experimental measurement.

Lewis Research Center,
National Aeronautics and Space Administration,
Cleveland, Ohio, April 17, 1968,
180-31-08-06-22.

APPENDIX A

SYMBOLS

A	area, ft^2; m^2
ΔA	incremental area, ft^2; m^2
$\mathscr{A}$	matrix of a system of finite-difference equations
a(x)	$(dN/dU)^{(k-1)}$
B	thermal buffer zone
$\mathscr{B}$	submatrices of order N which lie along diagonal of $\mathscr{A}$
b(x)	$NU^{(k-1)} - (dN/dU)^{(k-1)}U^{(k-1)}$
$\mathscr{C}$	off-diagonal submatrices of order N of $\mathscr{A}$
C_l	coefficients of eq. (B18) defined in eq. (B19), $l = 1, 2, \ldots, 5$
D	diameter, in.; cm
$\vec{d}$	vector whose components are right-hand sides of finite-difference equations
F	net radiation heat exchange factor between two gray bodies
G	$\omega/r\sigma$
I	position number of horizontal grid line
J	position number of vertical grid line
JEND	total number of vertical grid lines
$\overline{K}$	$k_B\left(\frac{T_{i,j-i} + T_{i,j}}{2}\right)$, used in finite-difference equations at interface
$\widetilde{K}$	$k_S\left(\frac{T_{i,j+1} + T_{i,j}}{2}\right)$, used in finite-difference equations at interface
k	thermal conductivity, Btu/(ft)(hr)(^oR); J/(m)(sec)(K)
N	number of shields
NJ	position number of interface vertical grid line
Q	heat flow, Btu/hr; J/sec
ΔQ	net increase in heat flow into tank, Btu/hr; J/sec
R	radius, in.; cm
r	radial coordinate
Δr	grid spacing in radial direction, in.; cm
T	temperature, ^oR; (K)
ΔT	temperature difference, ^oR; K
TCR	thermal contact resistance
U	pseudotemperature (transformed) in shield region
V	pseudotemperature (transformed) in buffer region

$\tilde{\tilde{V}}$	vector of pseudotemperature (transformed) in buffer region intermediate in the computation
$\overline{V}$	volume, ft^3; m^3
W	shield thickness, in.; cm
Z	insulation thickness, in.; cm
z	axial coordinate
Δz	grid spacing in axial direction, in.; cm
α	$F_{i,i+1}T^4_{i+1,r} + F_{i,i-1}T^4_{i-1,r}$
ϵ	emissivity
σ	Stefan-Boltzman constant, 0.173×10^{-8} Btu/(ft^2)(hr)$(^oR^4)$; 5.67×10^{-8} J/(m^2)(sec)(K^4)
τ	dummy variable
$\Delta\theta$	size of angular segment used as analytical model, deg
ω	block successive overrelaxation parameter

Subscripts:

avg	average
B	thermal buffer zone
cond	conduction
cs	cross section
dist	disturbed, or thermally degraded
e	shield edge
h	height
i	variable position in axial direction
int	buffer zone - shield interface
j	variable position in radial direction
lat	lateral
lh	liquid hydrogen
max	maximum
N	top shield position
nom	nominal
norm	normal direction
p	penetration
r	radial coordinate
rad	radiation
rs	radiating source
S	shield
tot	total
ts	thermally shorted
und	undisturbed
w	width

Superscripts:

(k)	k^{th} iterate
(m)	m^{th} iterate
(o)	initial approximation
$\rightarrow$	vector notation

APPENDIX B

NUMERICAL METHOD OF SOLUTION

The heat flow equations for the buffer (eq. (1)) and shield (eqs. (2)) regions are nonlinear, and the boundary conditions for these regions are also nonlinear. This precludes a closed-form solution so the problem was approached numerically.

One-to-one transformations were made as follows on equations (1) and (2) to eliminate the variable conductivity terms. Let

$$V(T) = \int_{T_{lh}}^{T} k_B(\tau)d\tau \tag{B1}$$

so that

$$\frac{dV}{dr} = k_B(T)\frac{dT}{dr} \tag{B2}$$

and

$$\frac{dV}{dz} = k_B(T)\frac{dT}{dz} \tag{B3}$$

Substituting equations (B2) and (B3) into equation (1) gives

$$\frac{\partial^2 V}{\partial r^2} + \frac{\partial^2 V}{\partial z^2} = 0 \tag{B4}$$

Similarly, let

$$U(T) = \int_{T_{lh}}^{T} k_S(\tau)d\tau \tag{B5}$$

then

$$\frac{dU}{dr} = k_S(T)\frac{dT}{dr} \tag{B6}$$

Note that in all the equations which follow, the dependence of T on U or V may not be explicitly stated.

Substituting equation (B6) into equations (2) gives

$$\left.\begin{aligned} W\frac{d}{dr}\left(r\frac{dU}{dr}\right) + r\sigma\left[F_{rs,N}T_{rs}^4 - (F_{rs,N} + F_{N,N-1})T_{N,r}^4 + F_{N,N-1}T_{N-1,r}^4\right] = 0 \\ W\frac{d}{dr}\left(r\frac{dU}{dr}\right) + r\sigma\left[F_{i,i+1}T_{i+1,r}^4 - (F_{i,i+1} + F_{i,i-1})T_{i,r}^4 + F_{i,i-1}T_{i-1,r}^4\right] = 0 \end{aligned}\right\} \quad (B7)$$

The transformations modify the boundary conditions. At $r = R_p$,

$$V(R_{p,z}) = V_p(T_p) \quad (B8)$$

The values of the dependent variables along the tank surface at $z = 0$ become

$$V = V(T_{lh}) = 0 \quad (B9)$$

and

$$U = U(T_{lh}) = 0 \quad (B10)$$

On the adiabatic boundary at $r = R_{dist}$,

$$\left(\frac{dU}{dr}\right)_{r=R_{dist}} = 0 \quad (B11)$$

The top surface at $z = z_{max}$ has the same boundary condition (eq. (6)) in the shield region as before the transformation

$$Q_{z=z_{max}} = F_{rs,N}\sigma\left(T_{rs}^4 - T_{N,r}^4\right) \quad (B12)$$

In the buffer region at $z = z_{max}$, equation (7) becomes

$$\left(\frac{\partial V}{\partial z}\right)_{z=z_{max}} = F_{rs,N}\sigma\left(T_{rs}^4 - T_{N,r}^4\right) \quad (B13)$$

At the interface, the equation for continuity of heat flow (eq. (8)) is now

$$\left(\frac{dV}{dr}\right)_{r=R_{int}} = \left(\frac{dU}{dr}\right)_{r=R_{int}} \tag{B14}$$

The numerical solution was obtained by replacing equations (B4) and (B7) by their finite-difference analogues at intersection points of a grid superimposed on the combined region of figure 4. These points are shown in figure 28. The solution of the differential

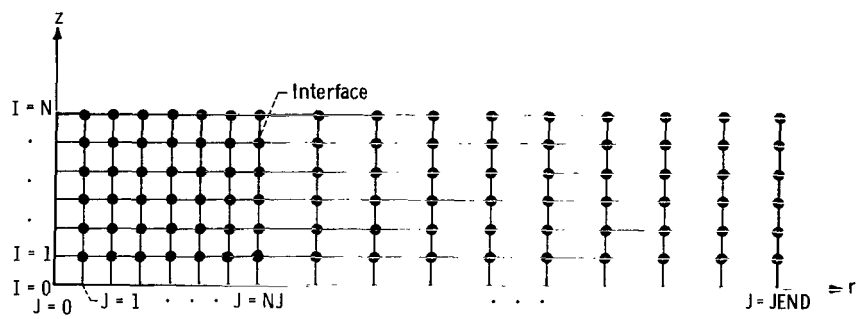

Figure 28. - Typical grid points where solution was obtained.

equations satisfies these difference equations except for an error term which vanishes when the grid spacing approaches zero.

As indicated in figure 28, each grid point has an ordered pair of integers (I,J) associated with it. The grid was constructed in such a way that each boundary - including the interface (J = NJ) - is a grid line. JEND is the total number of vertical grid lines and N is the total number of horizontal grid lines. The horizontals are uniformly spaced as are the verticals in the buffer region; the spacing of the verticals in the shield region is not necessarily uniform.

A dual grid was constructed in the buffer region by bisecting the grid lines in that region. This resulted in a closed cell about each point of the original grid. The boundaries of the cells are the dashed lines shown in figure 29.

The finite-difference equations for the pseudotemperatures (V) in the buffer were obtained as follows: (1) integrating equation (B4) over cells of the dual grid; (2) applying the divergence theorem; and (3) replacing the normal derivatives occurring in the boundary integrals by difference quotients, zero or $F_{rs,N}\sigma\left(T_{rs}^4 - T_{N,r}^4\right)$, depending on the position of the cell in question (ref. 4, sec. 6.3).

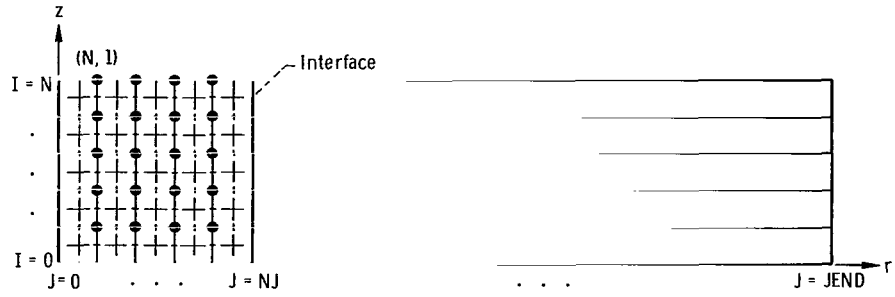

Figure 29. - Dual grid in buffer for numerical solution.

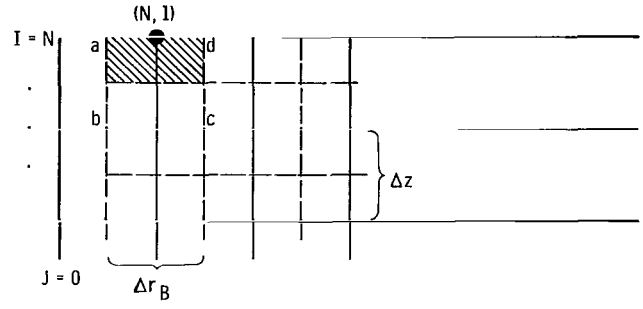

Figure 30. - Detail of grid for numerical solution in buffer.

The preceding process is illustrated by the following example taken at the point (I, J) = (N, 1) in figure 29. The cell of the dual grid under consideration (shaded in fig. 30) has its boundaries (except the upper one) midway between grid lines of the original grid. The finite-difference equation at the point (N, 1) is derived by the following steps where $i \equiv N$ and $j \equiv 1$:

$$0 = \int \left(\frac{\partial^2 V}{\partial r^2} + \frac{\partial^2 V}{\partial z^2} \right) d\bar{V}$$

$$0 = \int \frac{\partial V}{\partial n} \, dA$$

$$0 = \int_{a \to b} -\frac{\partial V}{\partial n} \, dA + \int_{b \to c} -\frac{\partial V}{\partial n} \, dA + \int_{c \to d} \frac{\partial V}{\partial n} \, dA + \int_{d \to a} \frac{\partial V}{\partial n} \, dA$$

$$0 \simeq \frac{V_p - V_{i,j}}{\Delta r_B} R_{j-(1/2)}\, \Delta\theta\, \frac{\Delta z}{2} + \frac{V_{i-1,j} - V_{i,j}}{\Delta z} R_j\, \Delta\theta\, \Delta r_B + \frac{V_{i,j+1} - V_{i,j}}{\Delta r_B} R_{j+(1/2)}\, \Delta\theta\, \frac{\Delta z}{2}$$

$$+ F_{rs,N}\sigma\left(T_{rs}^4 - T_{i,j}^4\right) R_j\, \Delta\theta\, \Delta r_B \qquad \text{(B15)}$$

The integration is repeated on all cells that surround the points (I,J) when $1 \le I \le N$ and $1 \le J \le NJ - 1$; this yields a system of $N(NJ - 1)$ equations in as many unknowns $V(I,J)$. Some $(NJ - 1)$ of these equations are nonlinear - namely (N,J), $1 \le J \le NJ - 1$.

Since this system cannot be solved directly because of the nonlinearity, an iterative procedure must be used. Let $V^{(m)}(I,J)$ represent the m^{th} iterate for $V(I,J)$ where $V^{(o)}(I,J)$ is some initial approximation to $V(I,J)$. Equations at the points (N,J), for $1 \le J \le NJ - 1$, are linearized by replacing the term $T^4(N,J)$ by the first two terms in its Taylor expansion about $V^{(m-1)}(N,J)$:

$$\left[T^{(m-1)}(N,J)\right]^4 + 4\left\{\frac{\left[T^{(m-1)}(N,J)\right]^3}{k_B\left[T^{(m-1)}(N,J)\right]}\right\}\left[V^{(m)}(N,J) - V^{(m-1)}(N,J)\right]$$

The resulting system of equations linear in $V^{(m)}$ can be written in matrix notation as

$$\mathscr{A}\vec{V}^{(m)} = \vec{d}$$

where

$$\mathscr{A} = \mathscr{A}\left(r_j;\ \vec{V}^{(m-1)}\right)$$

is a square matrix of order $N(NJ - 1)$ and

$$\vec{d} = \vec{d}\left(r_j;\ \vec{V}^{(m-1)}\right)$$

is a column vector with $N(NJ - 1)$ components. The block tridiagonal matrix $\mathscr{A}$ is given by

$$\mathcal{A} = \begin{pmatrix} \mathcal{B}_1 & -\mathcal{C}_1 & 0 & . & . & . & 0 & 0 \\ -\mathcal{C}_1 & \mathcal{B}_2 & -\mathcal{C}_2 & 0 & . & . & 0 & 0 \\ 0 & -\mathcal{C}_2 & \mathcal{B}_3 & . & . & . & . & . \\ . & 0 & -\mathcal{C}_3 & . & . & . & . & . \\ . & . & 0 & . & . & . & . & . \\ . & . & . & . & . & . & . & . \\ 0 & 0 & 0 & . & . & . & \mathcal{B}_{NJ-2} & -\mathcal{C}_{NJ-2} \\ 0 & 0 & 0 & . & . & . & -\mathcal{C}_{NJ-2} & \mathcal{B}_{NJ-1} \end{pmatrix}$$

Here

$$\mathcal{B}_J = \mathcal{B}\left[r_j;\ \vec{V}^{(m-1)}(N,J)\right] \qquad 1 \le J \le NJ - 1$$

are square tridiagonal matrices of order N, and

$$\mathcal{C}_J = \mathcal{C}\left(r_j;\ \vec{V}^{(m)}_{J-1};\ \vec{V}^{(m-1)}_{J+1}\right)$$

is a diagonal matrix of order N. The iterative method can be described as a line-by-line (vertical) overrelaxation scheme, which is carried out as follows.

An initial approximation to V is made at all points of the buffer region (e.g., $V^{(o)}(I,J) = V_p$). Then, V is changed by sweeping through these points an entire vertical at one time; that is, the V distribution at grid points on any one vertical is changed simultaneously. After a line is changed, the new V vector - denoted by $\tilde{\vec{V}}$ - is over-relaxed:

$$\vec{V}^{(m)}_J = \vec{V}^{(m-1)}_J + \omega\left(\tilde{\vec{V}}^{(m)}_J - \vec{V}^{(m-1)}_J\right)$$

where ω is the "block successive overrelaxation parameter" (ref. 4, ch. 4) that con-

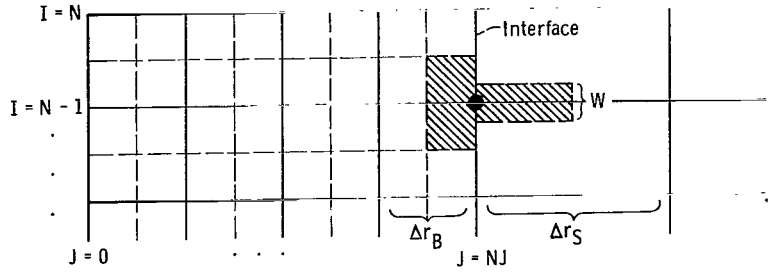

Figure 31. - Detail of grid for numerical solution at interface.

trols the rate of convergence. This scheme is applied to each line (vertical) moving from left to right - J = 1 through J = NJ - 1 - before working on the interface (J = NJ).

Figure 31 shows a typical cell on the interface surrounding the grid point (I, J) = (N - 1, NJ). Since the conductivity functions in the buffer and shield regions are different, the finite-difference equations for the point (N - 1, NJ) were written in terms of the temperature T.

Following a procedure analogous to that outlined on page 45 results in the following finite-difference equation for the point (N - 1, NJ) where $i \equiv N - 1$ and $j \equiv NJ$:

$$0 = \overline{K}_{i,j-(1/2)}(T_{i,j-1} - T_{i,j})r_{j-(1/2)}\,\Delta\theta\,\frac{\Delta z}{\Delta r_B}$$

$$+ \overline{K}_{i+(1/2),j}(T_{i+1,j} - T_{i,j})\left(r_j - \frac{1}{4}\Delta r_B\right)\frac{\Delta\theta\,\Delta r_B}{2\Delta z}$$

$$+ \overline{K}_{i-(1/2),j}(T_{i-1,j} - T_{i,j})\left(r_j - \frac{1}{4}\Delta r_B\right)\frac{\Delta\theta\,\Delta r_B}{2\Delta z}$$

$$+ \widetilde{K}_{i,j+(1/2)}(T_{i,j+1} - T_{i,j})\left(r_j + \frac{1}{2}\Delta r_S\right)\frac{\Delta\theta W}{\Delta r_S}$$

$$+ F_{i,i-1}\sigma\left(T^4_{i+1,j} - T^4_{i,j}\right)\left(r_j + \frac{1}{4}\Delta r_S\right)\frac{\Delta\theta\,\Delta r_S}{2}$$

$$+ F_{i,i-1}\sigma\left(T^4_{i-1,j} - T^4_{i,j}\right)\left(r_j + \frac{1}{4}\Delta r_S\right)\frac{\Delta\theta\,\Delta r_S}{2} \qquad \text{(B16)}$$

where

$$\left.\begin{aligned}\overline{K}_{i,j-(1/2)} &= k_B(T_{i,j-(1/2)}) = k_B\left(\frac{T_{i,j-1} + T_{i,j}}{2}\right)\\ \widetilde{K}_{i,j+(1/2)} &= k_S(T_{i,j+(1/2)}) = k_S\left(\frac{T_{i,j+1} + T_{i,j}}{2}\right)\end{aligned}\right\} \tag{B17}$$

typify the notation for the conductivity terms in equations (B16) and (B19).

The $T_{i,j}^4$ terms in equation (B16) must be linearized. Again, this is done by replacing $T_{i,j}^4$ by the first two terms in its Taylor expansion about $T_{i,j}^{(m-1)}$ - that is, by

$$\left(T_{i,j}^{(m-1)}\right)^4 + 4\left(T_{i,j}^{(m-1)}\right)^3\left(T_{i,j}^{(m)} - T_{i,j}^{(m-1)}\right)$$

which reduces to

$$4\left(T_{i,j}^{(m-1)}\right)^3 T_{i,j}^{(m)} - 3\left(T_{i,j}^{(m-1)}\right)^4$$

Substituting this last expression into equation (B16) and solving for $T_{i,j}^{(m)}$ gives

$$T_{i,j}^{(m)} = \frac{C_1T_{i,j-1} + C_2T_{i+1,j} + C_3T_{i-1,j} + C_4\left(T_{i+1,j}^4 + T_{i-1,j}^4\right) + 6C_4\left(T_{i,j}^{(m-1)}\right)^4 + C_5T_{i,j+1}}{C_1 + C_2 + C_3 + 8C_4\left(T_{i,j}^{(m-1)}\right)^3 + C_5} \tag{B18}$$

where

$$
\left.
\begin{aligned}
C_1 &= \overline{K}_{i,j-(1/2)}\, r_{j-(1/2)}\, \frac{\Delta z}{\Delta r_B} \\
C_2 &= \overline{K}_{i+(1/2),j}\left(r_j - \frac{1}{4}\Delta r_B\right)\frac{\Delta r_B}{2\Delta z} \\
C_3 &= \overline{K}_{i-(1/2),j}\left(r_j - \frac{1}{4}\Delta r_B\right)\frac{\Delta r_B}{2\Delta z} \\
C_4 &= F_{i,i-1}\sigma\left(r_j + \frac{1}{4}\Delta r_S\right)\frac{\Delta r_S}{2} \\
C_5 &= \widetilde{K}_{i,j+(1/2)}\left(r_j + \frac{1}{2}\Delta r_S\right)\frac{W}{\Delta r_S}
\end{aligned}
\right\} \qquad \text{(B19)}
$$

with $\Delta\theta$ eliminated.

Equation (B18) is in the point-Jacobi iterative form. Each point on the interface was relaxed by applying the successive overrelaxation scheme to the Jacobi method.

Resolving the heat-transfer problem in the shield region involved the solution of a system of nonlinear two-point boundary value problems. Consider only the second equation of equations (B7) since the following procedure is identical for the top shield (N); the only difference is one of notation. Rearranging this equation (where i represented the i^{th} shield) gives

$$
\frac{W}{r\sigma}\frac{d}{dr}\left(r\frac{dU}{dr}\right) + \left(F_{i,i+1}T^4_{i+1,r} + F_{i,i-1}T^4_{i-1,r}\right) = \left(F_{i,i+1} + F_{i,i-1}\right)T^4_{i,r} \qquad \text{(B20)}
$$

For simplicity, let

$$
G = \frac{W}{r\sigma} \qquad \text{(B21)}
$$

and

$$
\alpha = \left(F_{i,i+1}T^4_{i+1,r} + F_{i,i-1}T^4_{i-1,r}\right) \qquad \text{(B22)}
$$

Also for simplicity, the J verticals are renumbered so that J = 0 is the interface vertical and the last vertical is J = n (see fig. 32). Substituting equations (B21) and (B22) into (B20) yields

$$G\frac{d}{dr}\left(r\frac{dU}{dr}\right) + \alpha = \left(F_{i,i+1} + F_{i,i-1}\right)T_{i,r}^4 \tag{B23}$$

Equation (B23) was solved on each shield subject to the following boundary conditions. On the right (from eq. (B11)),

$$\left(\frac{dU}{dr}\right)_r = R_{dist} = 0 \tag{B24}$$

The left boundary of the shield region is the interface at $r = R_{int}$ where the U values are known at the m^{th} iteration as a function of the temperatures T at the m^{th} iteration; so on the left

$$U(R_{int,z}) = f(T,z) \tag{B25}$$

The solution was effected by applying Kalaba's linearization scheme (ref. 5) to equation (B23) and then integrating the result. The process just described was carried out as follows considering a general shield (i). Using Kalaba's method for linearization,

$$L(U) = N(U)$$

where L is a linear function and N is a nonlinear function, yields

$$L\left(U^{(k)}\right) = N\left(U^{(k-1)}\right) + \left(U^{(k)} - U^{(k-1)}\right)\left(\frac{dN}{dU}\right)^{(k-1)} \tag{B26}$$

where k represents the k^{th} iterate on the i^{th} shield.

Regrouping superscripts (k) in equation (B26) gives

$$L\left(U^{(k)}\right) - \left(\frac{dN}{dU}\right)^{(k-1)}U^{(k)} = N\left(U^{(k-1)}\right) - \left(\frac{dN}{dU}\right)^{(k-1)}U^{(k-1)} \tag{B27}$$

where the LHS is a function of coefficients evaluated at the previous iterate and the RHS is also a function of the previous iterate. Applying equation (B27) to equation (B23) gives

$$L(U) = G\frac{d}{dr}\left(r\,\frac{dU}{dr}\right) + \alpha$$

$$N\left[T(U)\right] = \left(F_{i,\,i+1} + F_{i,\,i-1}\right)\left[T(U_{i,\,r})\right]^4$$

$$\frac{dN}{dU} = 4\left(F_{i,\,i+1} + F_{i,\,i-1}\right)\left[T(U_{i,\,r})\right]^3 \frac{dT}{dU}$$

where

$$\frac{dT}{dU} = \frac{1}{k_S\left[T(U_{i,\,r})\right]}$$

which follows from equation (B6). Let

$$a(x) = \left(\frac{dN}{dU}\right)^{(k-1)}$$

and

$$b(x) = N\left(U^{(k-1)}\right) - \left(\frac{dN}{dU}\right)^{(k-1)} U^{(k-1)}$$

then, dropping superscripts k, equation (B23) becomes

$$G\frac{d}{dr}\left(r\,\frac{dU}{dr}\right) + \alpha - a(x)U = b(x) \qquad \text{(B28)}$$

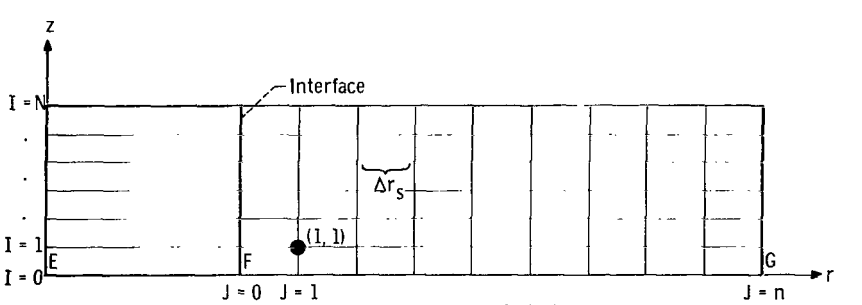

Figure 32. - Renumbering of shield verticals.

Consider the point $(i,j) = (1,1)$ where $j \equiv J$ (fig. 32). Integrating equation (B28) from $j - \frac{1}{2}$ to $j + \frac{1}{2}$ gives

$$\int_{j-(1/2)}^{j+(1/2)} G \frac{d}{dr}\left(r \frac{dU}{dr}\right) dr + \int_{j-(1/2)}^{j+(1/2)} \alpha \, dr - \int_{j-(1/2)}^{j+(1/2)} a(x)U \, dr = \int_{j-(1/2)}^{j+(1/2)} b(x) dr \qquad \text{(B29)}$$

and using central differences for the derivatives reduces equation (B29) to

$$r_{j-(1/2)} \, U_{j-1} - \left[2r_j + \frac{a(x_j)(\Delta r_S)^2}{G_j}\right] U_j + r_{j+(1/2)} \, U_{j+1} = \frac{\left[b(x_j) - \alpha_j\right](\Delta r_S)^2}{G_j} \qquad \text{(B30)}$$

Repeating the integration on equation (B28) for each point j, $1 \leq j \leq n$, and using the boundary values at the end points result in a system of n equations in n unknowns.

From equation (B30) and the statement following equation (B27), it can be seen that this is a system linear in $U^{(k)}$ which can be written in matrix notation as

$$A\vec{U}^{(k)} = \vec{d}$$

where

$$\mathscr{A} = \mathscr{A}\left(r_j; \vec{U}^{(k-1)}\right)$$

is a square tridiagonal matrix of order n and

$$\vec{d} = \vec{d}\left(r_j; U^{(k-1)}\right)$$

is a column vector of n components.

This system was also solved by the overrelaxation scheme applied to the line-by-line method. Each line (shield) was iterated on until the Euclidean norm of the U vector converged to within a tolerance of 0.01 percent.

After each line in the shield region - beginning with the shield closest to the tank wall and moving outward to the uppermost shield - was converged, the next overall $(m + 1)$ iteration was begun in the buffer region. This overall iteration was carried out until the relative residual error

$$\frac{|\text{heat in}| - |\text{heat out}|}{|\text{heat in}|}$$

was less than 0.001. Here

$$\text{heat in} = \int_{\substack{\text{Radiating} \\ \text{source} \\ \text{boundary}}} F_{rs,N}\sigma\left(T_{rs}^4 - T_{N,r}^4\right) dA$$

$$\text{heat out} = \int_{\text{Pipe}} k_B \frac{\partial T}{\partial n}\, dA + \int_E^F k_B \frac{\partial T}{\partial n}\, dA + \int_F^G k_S \frac{\partial T}{\partial n}\, dA$$

where E, F, and G are points on the tank surface shown in figure 32.

In the iterative methods described, the overrelaxation parameter ω is free to be chosen subject to the restriction $0 < \omega < 2$. It has been shown (ref. 4, ch. 4) for systems of linear equations that there is an optimum value of ω for which convergence is fastest. Because of the nonlinearity of the problem being considered here, no rigorous analysis exists for the determination of a corresponding optimum value of ω. Numerical experiments carried out at the Lewis Research Center, however, indicated the validity of the concept of an optimum value, and values of ω obtained in these experiments were used in the production runs. The result for a typical 40-shield case was $\omega = 1.85$ for 1840 points leading to convergence of the relative error in the heat balance to less than 0.1 percent in 248 iterations.

REFERENCES

1. Bonneville, Jacques M.: Design and Optimization of Space Thermal Protection for Cryogens-Analytic Techniques and Results. Rep. ADL-65958-02-01, Arthur D. Little, Inc. (NASA CR-54190), Dec. 18, 1964.

2. Anon.: Advanced Studies on Multi-Layer Insulation Systems. Rep. ADL-67180-00-04, Arthur D. Little, Inc. (NASA CR-54929), June 1, 1966.

3. Coston, R. M.: Handbook of Thermal Design Data for Multilayer Insulation Systems, Volume II. Rep. LMSC-A847882, Vol. II, Lockheed Missiles and Space Co. (NASA CR-87485), June 25, 1967.

4. Varga, Richard S.: Matrix Iterative Analysis. Prentice-Hall, Inc., 1962.

5. Kalaba, Robert: On Nonlinear Differential Equations, the Maximum Operation and Monotone Convergence. J. Math. Mech., vol. 8, no. 4, 1959, pp. 519-574.

"The aeronautical and space activities of the United States shall be conducted so as to contribute . . . to the expansion of human knowledge of phenomena in the atmosphere and space. The Administration shall provide for the widest practicable and appropriate dissemination of information concerning its activities and the results thereof."

—NATIONAL AERONAUTICS AND SPACE ACT OF 1958

NASA SCIENTIFIC AND TECHNICAL PUBLICATIONS

TECHNICAL REPORTS: Scientific and technical information considered important, complete, and a lasting contribution to existing knowledge.

TECHNICAL NOTES: Information less broad in scope but nevertheless of importance as a contribution to existing knowledge.

TECHNICAL MEMORANDUMS: Information receiving limited distribution because of preliminary data, security classification, or other reasons.

CONTRACTOR REPORTS: Scientific and technical information generated under a NASA contract or grant and considered an important contribution to existing knowledge.

TECHNICAL TRANSLATIONS: Information published in a foreign language considered to merit NASA distribution in English.

SPECIAL PUBLICATIONS: Information derived from or of value to NASA activities. Publications include conference proceedings, monographs, data compilations, handbooks, sourcebooks, and special bibliographies.

TECHNOLOGY UTILIZATION PUBLICATIONS: Information on technology used by NASA that may be of particular interest in commercial and other non-aerospace applications. Publications include Tech Briefs, Technology Utilization Reports and Notes, and Technology Surveys.

Details on the availability of these publications may be obtained from:

SCIENTIFIC AND TECHNICAL INFORMATION DIVISION

NATIONAL AERONAUTICS AND SPACE ADMINISTRATION

Washington, D.C. 20546